

Tin Whiskers:  
Crystal Plasticity Finite Element Modelling of Tin Crystals Using  
Phase Fields

Viktor Hultgren  
tfy14vhu@student.lu.se  
October 2018

# Contents

<b>1</b>	<b>Introduction</b>	<b>2</b>
1.1	Notation . . . . .	2
<b>2</b>	<b>Crystal Plasticity Model</b>	<b>3</b>
2.1	Introduction to Crystallographic Notation . . . . .	3
2.2	Crystal Plasticity Theory . . . . .	4
2.3	Plasticity Measure . . . . .	6
<b>3</b>	<b>Multi Phase Field Model</b>	<b>6</b>
3.1	Balance Equations . . . . .	7
3.2	Considering Thermodynamics . . . . .	8
3.3	Defining the Free Energy Functional and the Dissipation Potential . . . . .	10
3.3.1	The Interfacial Free Energy . . . . .	10
3.3.2	The Chemical Free Energy . . . . .	11
3.3.3	The Mechanical Free Energy . . . . .	11
3.3.4	The Dissipation Potential . . . . .	11
<b>4</b>	<b>Governing Equations of the Simulation</b>	<b>12</b>
<b>5</b>	<b>Numerical Trials</b>	<b>14</b>
5.1	Model Parameters . . . . .	14
5.1.1	Material Elastic and Plastic Parameters . . . . .	14
5.1.2	Temperature Dependent Parameters and Nucleation . . . . .	16
<b>6</b>	<b>Result and Discussion - Read remark</b>	<b>16</b>
6.1	Simulation where $Sn1$ is rotated using $\phi = 90^\circ, \psi = 30^\circ, \theta = 0^\circ$ . . . . .	17
6.2	Simulation where $Sn1$ is rotated using $\phi = 90^\circ, \psi = 30^\circ, \theta = 345^\circ$ . . . . .	19
6.3	Simulation where $Sn1$ is rotated using $\phi = 90^\circ, \psi = 30^\circ, \theta = 315^\circ$ . . . . .	22
6.4	Simulation where $Sn1$ is rotated using $\phi = 90^\circ, \psi = 75^\circ, \theta = 0^\circ$ . . . . .	24
6.5	Accumulated Plastic Slips of the Middle Tin Grain . . . . .	27
6.6	Discussion . . . . .	28
<b>7</b>	<b>Future Work</b>	<b>30</b>
<b>8</b>	<b>Conclusions</b>	<b>30</b>
<b>A</b>	<b>Appendix</b>	<b>32</b>
A.1	Slip systems used for the $\beta$ -tin grains. . . . .	32
A.2	Solving for the Hardening Parameters by Solving a System of PDE's . . . . .	33
<b>B</b>	<b>Calculation of Derivatives</b>	<b>33</b>
B.1	$f_{ch}$ . . . . .	34
B.2	$f_{int}$ . . . . .	34
B.3	$f_u$ . . . . .	34

## Acknowledgements

I want to thank both Matti Ristinmaa and Johan Hektor for supervising this project, and for helping me through all the various obstacles and conundrums which have appeared throughout the project. Having been able to stop by their offices whenever the work was leaving me wondering or when parameters were nowhere to be found has been a great relief. Additionally I am grateful to have been given the opportunity of visiting Idaho Falls to actually meet the persons behind the MOOSE software and attend a workshop held there in June 2018. Finally I also want to thank my fellow students in the "Library" together with the Solid Mechanics Department and all the employees there for for their wonderful company and advice.

# 1 Introduction

Tin whiskers have long caused issues to electronic components and made the subject of many articles. According to NASA the oldest reports concerning whiskers date back to the 1940's [3] with failures ranging from commercial satellites [8] to military equipment [6]. The whiskers are single-crystals growing from, for example electronic components. Despite the long history of tin whiskers the actual cause of their growth is still unknown. One of the reasons tin whiskers have gathered renewed attention during recent years is that formerly lead (Pb) was used in tin solders. Nowadays though, use of Pb is being restricted due to its toxicity, and for reasons unknown Pb seems to impair the growth of whiskers. Thus the issues caused by tin whiskers are more likely to occur with the new lead free solders [3]. The hypothesis held by the author is that the whiskers' growth is stress-driven by stresses originating from the formation of an inter metallic compound (IMC),  $\text{Cu}_6\text{Sn}_5$ , which forms due to a minimisation of the Gibbs free energy when mixing copper (Cu) and tin (Sn). Thus it is believed that the IMC will grow due to diffusion as the Cu, and Sn layers are in contact, with following transformation strains due to the volume change originating from the formation of the IMC. Another reason for the whisker growth might be that the thermal expansion coefficients are mismatched between the Sn and Cu causing stresses in the material [24], [25].

The need of incorporating crystal plasticity in the simulations is justified by the  $\beta$ -Sn crystal structure which is of body centred tetragonal type showing high anisotropy for elastic properties (c.f [13],[25]). This affects reliability of Sn based solder joints [5] as they may crack or deform. Moreover as the cause of the tin whisker growth is thought to be the stress building up it is paramount to accurately describe the growth process. Thus both of the IMC, and also of the corresponding stresses due to its growth, on a micro scale must be considered. This is done by employing multi phase fields as in [26], [1], and [18], to simulate the different grains and metals of a small system similar to [10]. The simulated system resembles a 2D profile of a solder with a Cu layer at the bottom and Sn on top. The IMC is then modelled to nucleate during an initial phase to mimic the fabrication of the solder. The aim with this work is to evaluate the effectiveness of simulating the tin whiskers growing: not from an imagined initial state where the IMC already has formed, but from a point where no IMC is originally present. With a successful simulation the IMC would be seen as it grows and during its formation, and one would be able to study the stress fields caused by it.

The chosen crystal plasticity model is a creep model, and thus plasticity is always present, even though it may be minuscule. The variables chosen to model the plasticity are the slips of the crystal planes and an increasing resistance to these slips. Dislocations due to slips are modelled through dislocation pile ups giving rise to a plastic potential within the crystal.

Moreover the crystal plasticity is presented for finite deformations whereas the phase field formulations and thus also the governing equations are presented in a small strain setting.

Lastly the simulations were performed in MOOSE [20] which is a FEM open source, multiphysics, software developed by Idaho National Laboratories. It is built upon C++ with libMesh and PETSc integrated to solve the differential equations at hand.

## 1.1 Notation

Throughout this thesis the following notation will be employed regarding tensor algebra and mathematics: Let  $\bar{e}_i$  denote the base vector, and let:  $\bar{a} = \sum_i a_i \bar{e}_i$ , denote a first order tensor,  $\bar{\bar{A}} = \sum_{i,j} A_{ij} \bar{e}_i \bar{e}_j$ , a second order tensor, and  $\bar{\bar{\bar{A}}} = \sum_{i,j,k,l} A_{ijkl} \bar{e}_i \bar{e}_j \bar{e}_k \bar{e}_l$  a fourth order tensor respectively.

$$\begin{aligned}
 \bar{a} \cdot \bar{b} &= \sum_i a_i b_i & \bar{a} \otimes \bar{b} &= \sum_{i,j} a_i b_j \bar{e}_i \bar{e}_j \\
 \bar{\bar{A}} : \bar{\bar{B}} &= \sum_{i,j} A_{ij} B_{ij} & \bar{\bar{A}} \cdot \bar{\bar{B}} &= \sum_{k,i,j} A_{ik} B_{kj} \bar{e}_i \bar{e}_j \\
 \bar{\bar{\bar{A}}} \cdot \bar{b} &= \sum_{i,j} A_{ij} b_j \bar{e}_i & \bar{\bar{\bar{A}}} : \bar{\bar{B}} &= \sum_{i,j,k,l} A_{ijkl} B_{kl} \bar{e}_i \bar{e}_j.
 \end{aligned}$$

Moreover ( $\dot{\square}$ ) will denote full time differentiation of the argument, and note that there is no sum over common indices in this work unless stated.

## 2 Crystal Plasticity Model

### 2.1 Introduction to Crystallographic Notation

With the aim of clarifying the following text some rudimentary notation is needed. When dealing with crystals the conventional unit cell is an effective tool to distinguish between various types of crystals. This cell is chosen as the minimal entity still retaining the symmetry of the underlying crystal lattice. The axes in the unit cell will be denoted  $\bar{a}$ ,  $\bar{b}$ , and  $\bar{c}$ . Let angles between two axes  $\bar{m}$  and  $\bar{n}$  be denoted  $[\bar{m}, \bar{n}]$ . Thus the angles between the different axes are denoted  $[\bar{a}, \bar{b}] = \gamma$ ,  $[\bar{b}, \bar{c}] = \alpha$ , and  $[\bar{c}, \bar{a}] = \beta$  spanning between the crystallographic axes (c.f. with the BCT unit cell of  $\beta$ -Sn in fig. (1)). The magnitude of each axis,  $|\bar{a}| = a$  etc., is called the lattice constants. To describe any direction within the cell the crystallographic coordinate system is used (c.f fig. (1)) and to denote the direction within a crystal lattice in a more compact format a bracket notation,  $[uvw]$ , is frequently used

$$\bar{m} = u\bar{a} + v\bar{b} + w\bar{c} \Leftrightarrow \bar{m} = [uvw], \quad (1)$$

where the convention is to scale  $\bar{m}$  sufficiently so that  $u$ ,  $v$ , and  $w$  are integer numbers. Should one have need of describing a negative direction it is denoted with an overhead bracket

$$\bar{m} = -\bar{a} + 2\bar{b} + \bar{c} \Leftrightarrow \bar{m} = [\bar{1}21]. \quad (2)$$

Furthermore the periodicity of the crystal often allows for an ever more compact format of the directions

$$\langle 101 \rangle \Leftrightarrow [101], [\bar{1}01], [10\bar{1}], [\bar{1}0\bar{1}], [011], [0\bar{1}1] \dots, \quad (3)$$

where the  $\langle \square \rangle$  notation is representing all possible sign and order permutations of the integers within the brackets which are equivalent after a symmetry operation (rotation about a lattice point, inversion, or mirroring about a axis) [23].

To denote crystal planes a notation similar to the one used for directions is employed called Miller indices. To obtain these in the case of a body centered tetragonal (BCT) crystal one may first construct a lattice plane by taking two vectors spanning a plane defined by three non-colinear Bravais sites [23]

$$\bar{q} = \bar{m} \cdot \bar{A} \text{ and } \bar{p} = \bar{n} \cdot \bar{A}; \text{ Let } \bar{A} = [\bar{a}, \bar{b}, \bar{c}]; \quad \bar{m}, \bar{n} \in \mathbb{R}^3. \quad (4)$$

The normal to this plane can be formed by taking the cross product of these vectors, and by remembering that the cross product of parallel vectors is the zero vector and that a right hand system is employed, the normal may be written

$$\bar{N} = \bar{q} \times \bar{p} = l_1 \bar{b} \times \bar{c} + l_2 \bar{c} \times \bar{a} + l_3 \bar{a} \times \bar{b}. \quad (5)$$

Omitting the full derivation as it is out of scope in this work one may define a reciprocal lattice as in [23] for reciprocal lattice vectors  $[\bar{a}^R, \bar{b}^R, \bar{c}^R]$ .

$$\begin{aligned} \bar{A}^R \cdot \bar{A} &= 2\pi \bar{I}; \quad \bar{A}^R = [\bar{a}^R, \bar{b}^R, \bar{c}^R], \\ \bar{a}^R &= \frac{2\pi}{V_C} (\bar{b} \times \bar{c}); \quad \bar{b}^R = \frac{2\pi}{V_C} (\bar{c} \times \bar{a}); \quad \bar{c}^R = \frac{2\pi}{V_C} (\bar{a} \times \bar{b}). \end{aligned} \quad (6)$$

In eq. (6),  $\bar{I}$  is denoting the unit tensor of order two, and recognizing that the volume of the unit cell is

$$V_C = \bar{a} \cdot (\bar{b} \times \bar{c}) = \bar{b} \cdot (\bar{c} \times \bar{a}) = \bar{c} \cdot (\bar{a} \times \bar{b}). \quad (7)$$

Using eq. (7) in combination with eq. (6) to rewrite eq. (5) into

$$\bar{N} = \frac{V_C}{2\pi} (l_1 \bar{a}^R + l_2 \bar{b}^R + l_3 \bar{c}^R) = h \cdot \bar{a}^R + k \cdot \bar{b}^R + l \cdot \bar{c}^R. \quad (8)$$

The indices  $h$ ,  $k$ , and  $l$  are chosen to be integers minimising the length of the vector  $\bar{N}$ . To utilize the symmetry of the crystal a notation using  $\{\square\}$  may also be used to denote a family of planes being equivalent after symmetry operations:

$$\{110\} = (110), (\bar{1}10), (1\bar{1}0), (\bar{1}\bar{1}0) \dots, \quad (9)$$

where the overhead bar once again denotes a negative integer. With the basic notation in place a slip system is defined by a slip plane  $(hkl)$  and a slip direction  $[uvw]$  as

$$(hkl)[uvw]. \quad (10)$$

Practically what one may do to interpret Miller indices denoting plane normals is to multiply the corresponding lattice vector with the reciprocal of the Miller index to obtain the corresponding intersection with that axis. Then one may rewrite the equation of the plane on its general form,  $\alpha x + \beta y + \gamma z + \epsilon = 0$ , using the three intersections as defining points of the plane. Then the Miller indices of the plane is given by the smallest set of the integers  $\alpha, \beta, \gamma$ .

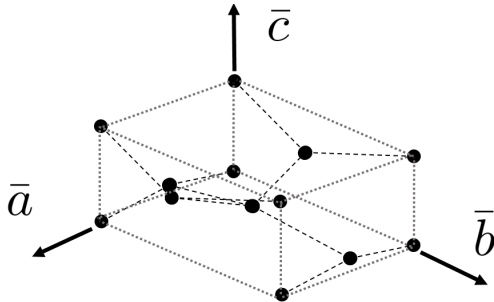


Figure 1: The BCT unit cell for  $\beta$ -Sn with marked lattice vectors.  $a = b = 5.8315 \text{ \AA}$ ,  $c = 3.1814 \text{ \AA}$  [14].

Furthermore it is used with the same argument as in [14] that the notation  $\langle hkl \rangle$  and  $\langle uvw \rangle$  recognises the tetragonal symmetry of the BCT crystal and means that the first two indices may permute and swap sign thus recovering all the slip systems of the family using compact notation. (c.f tab. (6))

Moreover when referring to a crystal, i.e. a region in a material with homogeneous orientation of its unit crystals, and thus having a uniform crystal lattice, the word grain may be used interchangeably. That is a piece of tin may consist of several grains, i.e. crystals.

## 2.2 Crystal Plasticity Theory

The model of the crystal plasticity is a phenomenological model relying on slips on crystal planes and an evolving resistance to these slips. The plastic dissipation is thought to arise from crystal plane friction resulting in heat losses. Moreover there are no grain boundaries in the model but of course crystal planes cannot slide forever and thus a dislocation pile up is modelled to give rise to an energy accumulation within the crystal. That is crystal planes eventually trapped at grain boundaries are incorporated into the model as a build up of plastic energy. To begin: let the deformation gradient be defined by

$$\bar{\bar{F}} = \frac{\partial \bar{x}}{\partial \bar{X}}, \quad (11)$$

where  $\bar{x}$  are the coordinates of a point lying within the crystal post deformation and  $\bar{X}$  is the same material point in the undeformed configuration. Now let the deformation gradient be split into two parts

$$\bar{\bar{F}} = \bar{\bar{F}}_e \cdot \bar{\bar{F}}_p. \quad (12)$$

In eq. (12)  $\bar{\bar{F}}_e$  denotes the elastic deformation gradient and  $\bar{\bar{F}}_p$  the plastic deformation gradient. The plastic deformation only considers slips in the crystal lattice which do not impose any change in angles between the crystal lattice planes. One could view it as a transformation into an intermediate configuration on which the elastic deformation gradient acts taking the domain to the final deformed state as in fig. (2). Now let the rate of change of the plastic deformation gradient be defined as in [17]

$$\dot{\bar{\bar{F}}}_p = \bar{\bar{L}}_p \cdot \bar{\bar{F}}_p = \left( \sum_{\alpha} \dot{\gamma}^{\alpha} \bar{\bar{S}}_0^{\alpha} \right) \cdot \bar{\bar{F}}_p = \left( \sum_{\alpha} \dot{\gamma}^{\alpha} \bar{\bar{m}}_0^{\alpha} \otimes \bar{\bar{n}}_0^{\alpha} \right) \cdot \bar{\bar{F}}_p. \quad (13)$$

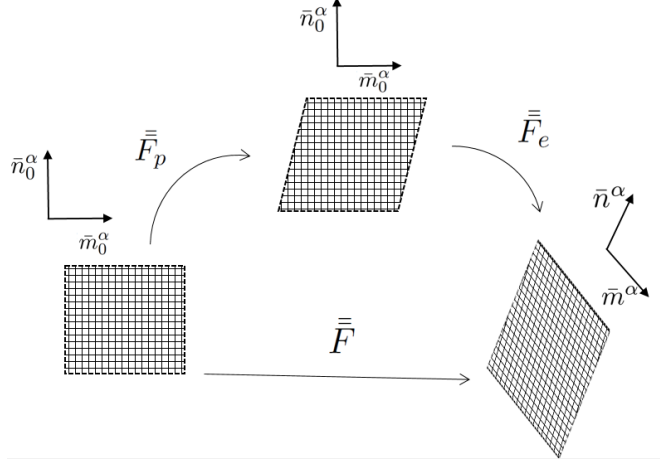


Figure 2: The different configurations corresponding to the factorization of the deformation gradient, with a slip system marked to see the shearing of the crystal slip planes due to elastic deformation.

Where in eq. (13)  $\alpha$  denotes a slip system of a total of  $N$  slip systems, and where the Schmidt tensor  $\bar{S}_0^\alpha$  is formed by a dyadic product between the slip direction  $\bar{m}_0^\alpha$ , and the slip plane normal  $\bar{n}_0^\alpha$  taken in the intermediate configuration  $\bar{\Omega}$ . In this configuration the slip planes and slip directions will be unchanged from the referential configuration,  $\Omega_0$ , (and in the laboratory basis  $\bar{e}_0$ ) based on the assumption that the slips do not create imperfections in the perfect crystal lattice.

Moreover  $\dot{\gamma}^\alpha$  denotes the flow rule of the of the crystal planes' plastic slips' which are, in line with [2], given by

$$\dot{\gamma}^\alpha = \dot{\gamma}_0 \left| \frac{\tau^\alpha}{s^\alpha} \right|^{1/m} \cdot \text{sgn}(\tau^\alpha); \quad \text{no sum on } \alpha, \quad (14)$$

where in eq. (14)  $\dot{\gamma}_0$  and  $m$  are an initial slip rate and a material constant controlling the material strain rate sensitivity [26]. Both are in this work taken to be equal for all slip systems.  $\tau^\alpha$  is the resolved shear stress on slip system  $\alpha$ , which is calculated by

$$\tau^\alpha = \bar{M} : \bar{S}_0^\alpha = \bar{m}_0^\alpha \cdot \bar{M} \cdot \bar{n}_0^\alpha; \quad \bar{M} = \bar{C}^e \cdot \bar{S}^e = \bar{C}^e \cdot \det(\bar{F}_e) \bar{F}_e^{-1} \cdot \bar{\sigma} \cdot \bar{F}_e^{-T}. \quad (15)$$

In eq. (15)  $\bar{C}^e$  is the right Cauchy-Green deformation tensor and  $\bar{S}^e$  is the second Piola-Kirchhoff stress tensor both taken in the intermediate configuration.  $\bar{M}$  is the Mandel stress tensor, and finally the Cauchy stress tensor is denoted  $\bar{\sigma}$ . The slip resistance,  $s^\alpha$ , is taken to evolve according to

$$\dot{s}^\alpha = \sum_{\beta}^N h^{\alpha\beta} |\dot{\gamma}^\beta|, \quad (16)$$

where, the hardening matrix,  $h^{\alpha\beta}$  in (16) is taken to be as in [26]

$$h^{\alpha\beta} = q^{\alpha\beta} h_0 \left| 1 - \frac{s^\beta}{\tau_{sat}^\beta} \right|^c \cdot \text{sgn}\left(1 - \frac{s^\beta}{\tau_{sat}^\beta}\right); \quad q^{\alpha\beta} = \begin{cases} 1.4, & \text{if } (\bar{n}_0^\alpha \nparallel \bar{n}_0^\beta), \\ 1, & \text{if } (\bar{n}_0^\alpha \parallel \bar{n}_0^\beta). \end{cases} \quad (17)$$

In (17)  $h_0$ ,  $\tau_{sat}^\beta$ , and  $c$  are material parameters which are constant.  $\tau_{sat}^\beta$  is the saturated slip resistance of slip system  $\beta$ .  $q^{\alpha\beta}$  is the latent hardening matrix where  $q^{\alpha\alpha}$  (no sum) corresponds to co-planar hardening and  $q^{\alpha\beta}$  corresponds to latent hardening [26]. Moreover it is thought that co-planar slips contribute less to the hardening i.e that  $q^{\alpha\beta}$  will have off diagonal coefficients as its largest values [21]. This also indicates the fact that all slips will affect the slip resistance for all the slip systems in a crystal and no such thing as a critical resolved shear stress is applicable as plasticity is initiated for all  $\tau^\alpha \neq 0$  [2] as this is a creep model.

It has been indicated in other works that certain slip systems in tin are more facile than others especially for slip systems with a slip direction aligned with the  $\bar{c}$  axis [14]. In contrast, as the model

present in this work does not rely on a critical resolved shear stress to initiate plasticity the ease at which a slip system is activated is not relevant. Rather one should expect greater plasticity for grains oriented in such a way that the projection of the shear stress onto the Schmidt tensor is large. As any slip system being subject to shear will in turn induce plasticity to all slip systems through the cross hardening of the crystal. Moreover tin is stiffest along the  $\bar{c}$  axis and most compliant in the  $\bar{a}-\bar{b}$  plane and there is a strong temperature dependence of these traits, which affect the degree of anisotropy between the directions [14].

Furthermore in [12] it is noted that for a hardening model similar to the one employed in this work:  $s_0^\alpha$ , i.e. the initial values of the slip resistances of each slip system affect the point at which the uni-axial stress-strain curves of the material goes into a non-linear regime.  $\tau_{sat}^\alpha$  affects the upper limit of the slip resistance and  $h_0$  is noticed to affect the initial hardening of the material. Lastly  $c$  will affect the shape between  $s_0^\alpha$  and  $\tau_{sat}^\alpha$  of the stress-strain curve.

### 2.3 Plasticity Measure

A measure of how the plasticity is developing is taken to be the  $\Delta\gamma_i^p$  of the matrix consisting of all the slips for each slip system for a material point. Let  $\Delta\gamma_i^p$  be defined as the matrix

$$\Delta\gamma_i^p = \Delta t \cdot \begin{bmatrix} \dot{\gamma}_i^1 \\ \dot{\gamma}_i^2 \\ \vdots \\ \dot{\gamma}_i^\alpha \\ \vdots \\ \dot{\gamma}_i^N \end{bmatrix}; \quad \Delta t := \text{an increment in time.} \quad (18)$$

$$\text{Then } \|\Delta\gamma_i^p\|_2 = \sqrt{\left(\sum_{k=1}^N \Delta t \dot{\gamma}_i^k \cdot \Delta t \dot{\gamma}_i^k\right)} = \Delta t \cdot \sqrt{\left(\sum_{k=1}^N \dot{\gamma}_i^k \cdot \dot{\gamma}_i^k\right)}. \quad (19)$$

In eq. (18)  $\dot{\gamma}_i^\alpha$ , is the slip rate in phase  $i$  for slip system  $\alpha = \{1, 2, \dots, N\}$ . The slip rate multiplied with  $\Delta t$  will result in a slip increment which if sampled as a field over the domain will show which areas are being plasticised in the current step. Accumulating this variable will provide a measurement of the total plasticity over the domain over the given time period and this measurement will be defined as

$$\gamma_i^{tot} = \sum_{t_0}^t (\|\Delta\gamma_i^p\|_2). \quad (20)$$

With this choice  $\gamma_i^{tot}$  will thus contain an overview of the plastic history of the material.

## 3 Multi Phase Field Model

To be able to describe the multiple grains present in the simulation, this work employs the method used by [10], in which a phase field having a diffusive interface is assigned to every crystal. Thus the poly-crystal of the simulation is described by phase field variables dependent on the spatial coordinates  $\bar{r}$  and the time  $t$ .

$$\phi = [\phi_a(t, \bar{r}), \phi_b(t, \bar{r}), \dots, \phi_n(t, \bar{r})]^T, \quad (21)$$

In (21) a phase field variable  $\phi_a$  is assigned to every grain for all grains  $1, 2, \dots, b, \dots, n$  for  $n$  grains. Where two phases intersect the phase field variables of the two grains will vary smoothly  $0 < \phi_i < 1$ . The distance over which this occurs is referred to as the diffuse interface region.



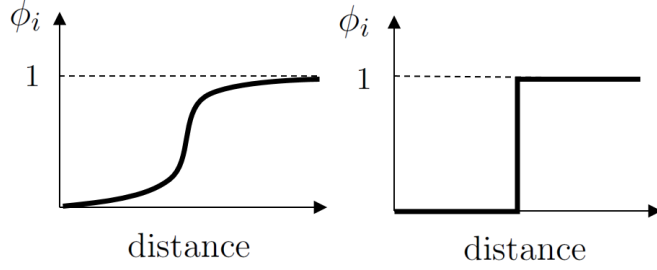


Figure 3: To the left a diffuse interface is shown, varying smoothly between 0 and 1 over the diffuse region width. To the right for comparison is a sharp interface formulation.

Over the entire domain the phase field variables,  $\phi$ , are interpolated so as to decide the proper weight of the phases. The formulation used by [18] for the interpolation functions deciding this weighting will be used in this work

$$h_i(\phi) = \frac{\phi_i^2}{\sum_j^n \phi_j^2}. \quad (22)$$

and  $h_i$  will hereby represent the various phases present in the domain and they will have the property of summing up to 1 at every point of the domain. This trait is not necessarily true for the phase field variables.

Following the choice of [10] in describing the diffusion: conserved field variables are introduced representing the molar fraction in each grain.

$$\mathbf{x} = (x_a(t, \bar{r}), x_b(t, \bar{r}), \dots, x_n(t, \bar{r})) \quad (23)$$

The global molar concentration field depends on the molar fractions in each grain through the relation seen in (24)

$$c = \sum_{a=1}^n h_a \frac{x_a}{V_m} \quad (24)$$

which shows how the interpolation functions build up the macroscopic concentration by summation of the concentrations present in each phase. In (24),  $V_m$ , denotes a constant molar volume, and  $h_a$  is the interpolation function formulated in (22).

### 3.1 Balance Equations

Following [1] by recognising that for any subdomain,  $\mathcal{D}$ , belonging to a body  $\mathcal{V}$  together with any admissible virtual displacements  $\bar{u}^*$  and any virtual phases  $\phi^*$  three virtual power densities are assumed to be admitted at any point within  $\mathcal{V}$  for phases  $i = 1, 2, \dots, n$ . Namely, virtual power originating from external generalized forces ( $e$ ), contact ( $c$ ) and from internal generalized forces ( $i$ ) denoted as

$$p^{(e)}(\phi^*, \bar{u}^*); p^{(c)}(\phi^*, \bar{u}^*) \text{ and } p^{(i)}(\phi^*, \bar{u}^*); \quad \phi^* = [\phi_1^*, \phi_2^*, \dots, \phi_n^*]^T. \quad (25)$$

A set of generalised stresses  $\{-\pi, \bar{\xi}, \bar{\sigma}\}$  are introduced power conjugate to the set  $\{\phi^*, \bar{\nabla}\phi^*, \nabla\bar{u}^*\}$ , letting the star denote virtual quantities. Let  $\bar{\xi}$  denote the vector micro stress and  $-\pi$  is the scalar micro stress whereas  $\bar{\sigma}$  is the Cauchy stress tensor. The virtual power density originating from external generalised forces becomes

$$p^{(e)}(\phi^*, \bar{u}^*) = \sum_i (\gamma_i \phi_i^*) + \bar{b} \cdot \bar{u}^*. \quad (26)$$

Where  $\bar{b}$  is denoting body forces and  $\gamma_i$  are denoting external micro forces. The virtual power density which stem from the internal generalised forces is written

$$p^{(i)}(\phi^*, \bar{u}^*) = \sum_i (\pi_i \phi_i^* + \bar{\xi}_i \cdot \bar{\nabla}\phi_i^* - \bar{\sigma}_i : \nabla\bar{u}^*). \quad (27)$$

Lastly the virtual power density caused by contact reads

$$p^{(c)}(\boldsymbol{\phi}^*, \bar{\mathbf{u}}^*) = \sum_i (\vartheta_i \phi_i^*) + \bar{\mathbf{t}} \cdot \bar{\mathbf{u}}^*, \quad (28)$$

where  $\vartheta_i$  is the density of surface micro tractions in each phase and where  $\bar{\mathbf{t}}$  is the traction: both of which act on  $\partial\mathcal{V}$ .

Now, not considering any inertial micro forces, according to the principle of virtual power that in  $\mathcal{V}$ , for any admissible  $\phi_i^*$  and  $\bar{\mathbf{u}}^*$ , the virtual power of the domain must be balanced:

$$\int_{\mathcal{V}} \left( p^{(e)}(\boldsymbol{\phi}^*, \bar{\mathbf{u}}^*) + p^{(i)}(\boldsymbol{\phi}^*, \bar{\mathbf{u}}^*) \right) dV + \int_{\partial\mathcal{V}} p^{(c)}(\boldsymbol{\phi}^*, \bar{\mathbf{u}}^*) dS = \quad (29)$$

$$= \int_{\mathcal{V}} \left( \bar{\mathbf{b}} \cdot \bar{\mathbf{u}}^* + \sum_i (\gamma_i \phi_i^* + \pi_i \phi_i^* + \bar{\boldsymbol{\xi}}_i \cdot \nabla \phi_i^* - \bar{\boldsymbol{\sigma}}_i : \nabla \bar{\mathbf{u}}^*) \right) dV + \quad (30)$$

$$+ \int_{\partial\mathcal{V}} \left( \bar{\mathbf{t}} \cdot \bar{\mathbf{u}}^* + \sum_i (\vartheta_i \phi_i^*) \right) dS = 0$$

Using the following identities applicable to each phase  $i$

$$\int_{\mathcal{V}} \bar{\boldsymbol{\xi}}_i \cdot \nabla \phi_i^* = \int_{\mathcal{V}} (\nabla \cdot (\bar{\boldsymbol{\xi}}_i \phi_i^*) - (\nabla \cdot \bar{\boldsymbol{\xi}}_i) \phi_i^*) dV = - \int_{\mathcal{V}} (\nabla \cdot \bar{\boldsymbol{\xi}}_i) \phi_i^* dV + \int_{\partial\mathcal{V}} \bar{\boldsymbol{\xi}}_i \phi_i^* \cdot \bar{\mathbf{n}} dS;$$

$$\int_{\mathcal{V}} \bar{\boldsymbol{\sigma}}_i : \nabla \bar{\mathbf{u}}^* = \int_{\mathcal{V}} (\nabla \cdot (\bar{\boldsymbol{\sigma}}_i \cdot \bar{\mathbf{u}}^*) - (\nabla \cdot \bar{\boldsymbol{\sigma}}_i) \cdot \bar{\mathbf{u}}^*) dV =$$

$$= - \int_{\mathcal{V}} (\nabla \cdot \bar{\boldsymbol{\sigma}}_i) \cdot \bar{\mathbf{u}}^* dV + \int_{\partial\mathcal{V}} ((\bar{\boldsymbol{\sigma}}_i \cdot \bar{\mathbf{n}}) \cdot \bar{\mathbf{u}}^*) dS$$

It follows that eq. 30 may be rewritten into

$$\int_{\mathcal{V}} \left( \bar{\mathbf{b}} \cdot \bar{\mathbf{u}}^* + \sum_i ((\pi_i + \gamma_i + \nabla \cdot \bar{\boldsymbol{\xi}}_i) \phi_i^* + (\nabla \cdot \bar{\boldsymbol{\sigma}}_i) \cdot \bar{\mathbf{u}}^*) \right) dV + \quad (31)$$

$$\int_{\partial\mathcal{V}} \left( \bar{\mathbf{t}} \cdot \bar{\mathbf{u}}^* + \sum_i ((\vartheta_i - \bar{\boldsymbol{\xi}}_i \cdot \bar{\mathbf{n}}) \phi_i^* - (\bar{\boldsymbol{\sigma}}_i \cdot \bar{\mathbf{n}}) \cdot \bar{\mathbf{u}}^*) \right) dS = 0.$$

From eq. (31) it is deduced, from the choice that  $\phi_i^*$  and  $\bar{\mathbf{u}}^*$  may vary independently, both integrands must equal zero termwise: producing the following balance equations and boundary conditions

$$\text{in } \mathcal{V} : \begin{cases} \sum_i (\bar{\nabla} \cdot \bar{\boldsymbol{\xi}}_i + \pi_i + \gamma_i) = 0, \\ \sum_i (\bar{\nabla} \cdot \bar{\boldsymbol{\sigma}}_i) + \bar{\mathbf{b}} = \bar{\mathbf{0}}; \end{cases} \quad \text{on } \partial\mathcal{V} : \begin{cases} \sum_i (\vartheta_i - \bar{\boldsymbol{\xi}}_i \cdot \bar{\mathbf{n}}) = 0, \\ \sum_i (-\bar{\boldsymbol{\sigma}}_i \cdot \bar{\mathbf{n}}) + \bar{\mathbf{t}} = \bar{\mathbf{0}}. \end{cases} \quad (32)$$

### 3.2 Considering Thermodynamics

Now dropping the  $(\cdot)^*$  and assuming that an admissible set of order variables  $\boldsymbol{\phi}$ , and displacements  $\bar{\mathbf{u}}$ , are present: the variation of the internal energy  $\mathcal{U}$  can be described with the help of the principle of virtual work

$$\mathcal{U}(\boldsymbol{\phi}, \bar{\mathbf{u}}, t) = \int_{\mathcal{V}} p^{(e)}(\boldsymbol{\phi}, \bar{\mathbf{u}}) dV + \int_{\partial\mathcal{V}} p^{(c)}(\boldsymbol{\phi}, \bar{\mathbf{u}}) dS$$

$$= - \int_{\mathcal{V}} (p^{(i)}(\boldsymbol{\phi}, \bar{\mathbf{u}})) dV. \quad (33)$$

The variation of the internal energy can be formulated, and analogous to [1] the variation is stated assuming no acceleration effects and with absence of thermal effects.

$$\dot{\mathcal{U}} = \int_{\mathcal{V}} \dot{e} dV = - \int_{\mathcal{V}} p^{(i)}(\dot{\boldsymbol{\phi}}, \dot{\bar{\mathbf{u}}}) dV. \quad (34)$$

Where in eq. (34)  $\dot{e}$  is the variation of the internal energy, and by taking advantage of (27) may be expressed as

$$\dot{e} = \sum_i \left( -\pi_i \dot{\phi}_i + \bar{\xi}_i \cdot \nabla \dot{\phi}_i + \bar{\sigma}_i : \dot{\bar{\varepsilon}} \right) \quad (35)$$

in which  $\bar{\varepsilon}$  is the strain which, in accordance with the Voigt-Taylor assumption [11] may be split into

$$\bar{\varepsilon} = \bar{\varepsilon}_i^{(e)} + \bar{\varepsilon}_i^{(p)} + \bar{\varepsilon}_i^{(0)}. \quad (36)$$

In eq. (36)  $\bar{\varepsilon}_i^{(e)}$  denotes the elastic strain,  $\bar{\varepsilon}_i^{(p)}$  the plastic strain, and  $\bar{\varepsilon}_i^{(0)}$  denotes the transformation strain in phase  $i$ . Practically this states that the total strain in any incremental volume will be the same in all phases. Especially this concerns interfaces where the different phases overlap. This also implies that different stress states, and thus different states of plasticity are allowed among the phases within the same incremental volume. Note that the strain is assumed to be small and thus linear in displacements.

Assuming an irreversible process the second law of thermodynamics states that the diffusion induced rate of the entropy flux may never exceed the variation of entropy. Thus for a temperature  $T$ , entropy  $s$ , chemical potential  $\mu$  and a diffusion flux  $\bar{J}$  it must hold that

$$T\dot{s} - \nabla \cdot (\mu\bar{J}) \geq 0. \quad (37)$$

With the use of the continuity equation (mass balance)

$$\dot{c} = -\nabla \cdot \bar{J}, \quad (38)$$

and introducing a free energy density,

$$\dot{f}(\phi, \nabla\phi, c, \bar{\varepsilon}_i^{(e)}, \kappa_i) = \dot{e} - T\dot{s}; \quad \nabla\phi = [\nabla\phi_1, \nabla\phi_2, \dots, \nabla\phi_n]^T; \quad \kappa_i = [\kappa_i^1, \kappa_i^2, \dots, \kappa_i^N]^T, \quad (39)$$

its time variation can be rewritten using the product rule

$$\dot{f} = \frac{\partial f}{\partial c} \dot{c} + \sum_i \left( \frac{\partial f}{\partial \phi_i} \dot{\phi}_i + \frac{\partial f}{\partial \nabla \phi_i} \cdot \nabla \dot{\phi}_i + \frac{\partial f}{\partial \bar{\varepsilon}_i^{(e)}} : \dot{\bar{\varepsilon}}_i^{(e)} + \left( \frac{\partial f}{\partial \kappa_i} \right)^T \dot{\kappa}_i \right). \quad (40)$$

In eq. (40),  $\kappa_i^\alpha$ ;  $\alpha = 1, 2, \dots, N$ , are internal variables related to plasticity of each phase.

With the use of eq. (38) and (40), eq. (37) is rewritten into the Clausius-Duhem inequality

$$\dot{e} - \dot{f} - \nabla \cdot (\mu\bar{J}) \geq 0, \quad (41)$$

and insertion of eqs. (35) and (40) provides

$$\begin{aligned} & \sum_i \left[ - \left( \pi_i + \frac{\partial f}{\partial \phi_i} \right) \dot{\phi}_i + \left( \bar{\xi}_i - \frac{\partial f}{\partial \nabla \phi_i} \right) \cdot \nabla \dot{\phi}_i \right] \\ & + \sum_i \left[ \left( \bar{\sigma}_i - \frac{\partial f}{\partial \bar{\varepsilon}_i^{(e)}} \right) : \dot{\bar{\varepsilon}}_i^{(e)} + \bar{\sigma}_i : \dot{\bar{\varepsilon}}_i^{(p)} + \bar{\sigma}_i : \dot{\bar{\varepsilon}}_i^{(0)} - \left( \frac{\partial f}{\partial \kappa_i} \right)^T \dot{\kappa}_i \right] - \nabla \mu \cdot \bar{J} + \left( \mu - \frac{\partial f}{\partial c} \right) \dot{c} \geq 0. \end{aligned} \quad (42)$$

Following [10], state laws are obtained for the chemical potential, the Cauchy stress, and the internal micro stress by demanding eq. (41) to hold for any variation of  $\{\dot{c}, \dot{\bar{\varepsilon}}_i^{(e)}, \nabla \dot{\phi}_i\}$

$$\mu = \frac{\partial f}{\partial c}, \quad \bar{\sigma}_i = \frac{\partial f}{\partial \bar{\varepsilon}_i^{(e)}}, \quad \bar{\xi}_i = \frac{\partial f}{\partial \nabla \phi_i}. \quad (43)$$

Next introducing dissipative micro stresses  $\pi_i^{dis}$  and hardening functions  $K_i^\alpha$  are introduced as

$$\pi_i^{dis} = \pi_i + \frac{\partial f}{\partial \phi_i}, \quad K_i^\alpha = \frac{\partial f}{\partial \kappa_i^\alpha}, \quad (44)$$

and by inserting the state laws of eq. (43) into eq. (41) and defining the matrix,  $\mathbf{K}_i = [K_i^1, K_i^2, \dots, K_i^N]^T$ , the dissipation inequality is obtained

$$D = - \sum_i \left( \pi_i^{dis} \dot{\phi}_i + \bar{\sigma}_i : \dot{\bar{\varepsilon}}_i^{(p)} - \mathbf{K}_i^T \dot{\boldsymbol{\kappa}}_i \right) - \nabla \mu \cdot \bar{J} \geq 0. \quad (45)$$

Moving on: three dissipative processes can be identified in eq. (45) where the first term is related to the phase field dissipation. The second and third term originates from plastic deformation and the fourth and last term relates to flux of atoms.

In analogy with [10] the dissipative terms in eq. (45) are assumed to stem from a convex dissipation potential,  $\Omega(\boldsymbol{\pi}^{(dis)}, \phi, c, \nabla \mu, \bar{\sigma}_i, \mathbf{K}_i)$ , in such a way that the following holds

$$\dot{\phi}_i = \frac{\partial \Omega}{\partial \pi_i^{(dis)}}, \quad (46)$$

$$\bar{J} = - \frac{\partial \Omega}{\partial \nabla \mu}, \quad (47)$$

$$\dot{\boldsymbol{\kappa}}_i^\alpha = - \dot{\lambda}_i \frac{\partial \Omega}{\partial K_i^\alpha}, \quad \dot{\lambda}_i \geq 0 \quad (48)$$

$$\dot{\bar{\varepsilon}}_i^{(p)} = \dot{\lambda}_i \frac{\partial \Omega}{\partial \bar{\sigma}_i}, \quad \dot{\lambda}_i \geq 0. \quad (49)$$

Thus the evolution of the phase fields  $i = 1, \dots, n$  is given by eq. (46). In eq. (47) the flux is provided. Lastly  $\lambda_i$  in eq. (48) and (49) is a plastic multiplier associated with plastic deformation for phase  $i$  and the equations enable computation of the internal variables associated with each phase's plasticity.

### 3.3 Defining the Free Energy Functional and the Dissipation Potential

As mentioned in [19] the free energy functional is required to describe the driving force of the phase field variables. Here the elastoplastic behaviour of the material is presented as well as the the previously mentioned dissipation potential. Following [10] first the free energy,  $F$ , is defined by integration of the free energy density within the domain  $\mathcal{V}$

$$F = \int_{\mathcal{V}} f(\phi, \nabla \phi, c, \bar{\varepsilon}_i^{(e)}, \boldsymbol{\kappa}_i) dV, \quad (50)$$

and subsequently identifying three terms: the chemical,  $f_{ch}$ , the mechanical,  $f_u$  and the interfacial,  $f_{int}$ , energy forming the free energy density

$$f(\phi, \nabla \phi, c, \bar{\varepsilon}_i^{(e)}, \boldsymbol{\kappa}_i) = f_{ch}(\phi, c) + f_{int}(\phi, \nabla \phi) + f_u(\phi, c, \bar{\varepsilon}_i^{(e)}, \boldsymbol{\kappa}_i) \quad (51)$$

#### 3.3.1 The Interfacial Free Energy

Proceeding as in [18] and [10] the interfacial free energy is taken as

$$f_{int} = a_1^{int} f_0(\phi) + \frac{a_2^{int}}{2} \sum_i (\nabla \phi_i)^2, \quad (52)$$

where  $f_0$  is taken to be a fourth order Landau polynomial

$$f_0(\phi) = \sum_i \left( \frac{\phi_i^4}{4} - \frac{\phi_i^2}{2} \right) + \sum_i \sum_{j \neq i} \left( \frac{a_3^{int}}{2} \phi_i^2 \phi_j^2 \right) + \frac{1}{4}. \quad (53)$$

In eq:s (52) and (53) the parameters  $a_i^{int}$ ,  $i = 1, 2, 3$ , are dependent upon the surface energy  $\sigma^{int}$  and the diffuse interface region width  $\delta$

$$a_1^{int} = \frac{6\sigma^{int}}{\delta}; \quad a_2^{int} = \frac{3\sigma^{int}\delta}{4}; \quad a_3^{int} = \frac{3}{2} \quad (54)$$

Moreover in [10] the choice of the function  $f_0$  is motivated by the locations of minimas of the polynomials. These are located in the interior of each phase where the function will be zero and thus only the boundaries contribute to the energy stored by interfaces.

### 3.3.2 The Chemical Free Energy

In analogy with [18] the chemical free energy is expressed as

$$f_{ch} = \sum_i h_i \frac{G_i(x_i)}{V_m} \quad (55)$$

where  $h_i$  are the interpolation functions seen in eq. (22),  $G_i$  is the molar Gibbs energy for the phase  $i$ , and  $V_m$  is the molar volume. Similar as in [9],  $G_i$  is approximated with the parabola

$$G_i = \frac{a_{1:i}^G}{2} (x_i - \hat{x}_i)^2 + a_{2:i}^G (x_i - \hat{x}_i) + a_{3:i}^G, \quad (56)$$

with the parameters

$$a_{1:i}^G = \left. \frac{d^2 \hat{G}_i}{dx_i^2} \right|_{x_i = \hat{x}_i}; \quad a_{2:i}^G = \left. \frac{d \hat{G}_i}{dx_i} \right|_{x_i = \hat{x}_i}; \quad a_{3:i}^G = \hat{G}_i \Big|_{x_i = \hat{x}_i}. \quad (57)$$

The parameters in eq. (57) are functions of the composition dependent Gibbs energy,  $\hat{G}_i$ . In eq. (56) and eq. (57),  $\hat{x}_i$  denotes the equilibrium molar fraction of phase  $i$ .

### 3.3.3 The Mechanical Free Energy

Following [10] by splitting  $f_u$  into an elastic part,  $f^{(e)}$  and a plastic part,  $f^{(p)}$

$$f_u(\boldsymbol{\phi}, c, \bar{\bar{\varepsilon}}_i^{(e)}, \boldsymbol{\kappa}_i) = f^{(e)}(\boldsymbol{\phi}, c, \bar{\bar{\varepsilon}}_i^{(e)}) + f^{(p)}(\boldsymbol{\phi}, c, \boldsymbol{\kappa}_i), \quad (58)$$

Once again the Voigt-Taylor assumption [11] is used to homogenize the strain at phase intersections in conjunction with an assumption of hyper elasticity of phase  $i$ , i.e.

$$f^{(e)} = \sum_i h_i f_i^{(e)} = \frac{1}{2} \sum_i h_i \left( (\bar{\bar{\varepsilon}} - (\bar{\bar{\varepsilon}}_i^{(p)} + \bar{\bar{\varepsilon}}_i^{(0)})) : \bar{\bar{\mathbb{D}}}_i : (\bar{\bar{\varepsilon}} - (\bar{\bar{\varepsilon}}_i^{(p)} + \bar{\bar{\varepsilon}}_i^{(0)})) \right), \quad (59)$$

where the relation seen in eq. (36) have been used to replace  $\bar{\bar{\varepsilon}}_i^{(e)}$  and where  $\bar{\bar{\mathbb{D}}}_i$  is a fourth order constitutive tensor corresponding to the material present in phase  $i$ .

The plastic free energy is modelled as in [17], with the addition of the interpolation of the phases

$$f^{(p)} = \sum_i h_i f_i^{(p)} = \sum_i h_i \left[ \frac{Q_i}{2} \sum_{\alpha} \sum_{\beta} q_i^{\alpha\beta} s_i^{\alpha} s_i^{\beta} \right] \quad (60)$$

where  $Q_i$  are material parameters. Moreover  $q^{\alpha\beta}$ , can be seen in eq. (17) and controls the hardening between slip systems that are coplanar and the cross hardening of slip systems.

### 3.3.4 The Dissipation Potential

Returning to the previously mentioned dissipation potential (eq:s (46)-(49)) splitting it into three terms

$$\Omega(\boldsymbol{\pi}^{dis}, \boldsymbol{\phi}, c, \nabla \mu, \bar{\bar{M}}_i, \bar{\bar{L}}_i^p, \mathbf{K}_i, \boldsymbol{\kappa}_i) = \Omega_{ch}(\nabla \mu) + \Omega_{\phi}(\boldsymbol{\pi}^{dis}) + \Omega_u(\boldsymbol{\phi}, c, \bar{\bar{M}}_i, \bar{\bar{L}}_i^p, \mathbf{K}_i, \boldsymbol{\kappa}_i). \quad (61)$$

Where as in [1] the chemical dissipation,  $\Omega_{ch}$  is taken to be

$$\Omega_{ch}(\nabla \mu) = \frac{1}{2} M(\boldsymbol{\phi}) (\nabla \mu)^2. \quad (62)$$

In eq. (62)  $M(\boldsymbol{\phi})$  is the mobility modelled as

$$M(\boldsymbol{\phi}) = \sum_i \frac{h_i}{V_m} \left( \frac{D_i}{\frac{d^2 G_i}{dx_i^2}} + \sum_{j \neq i} h_j M_{gb} \right) \quad (63)$$

where,  $D_i$  is the diffusion coefficient of phase  $i$ , and in analogy with [10],

$$M_{gb} = 3 \frac{D_{gb}}{h_i a_{1:i}^G + h_j a_{1:j}^G} \frac{\delta_{gb}}{\delta}, \quad (64)$$

is the grain boundary mobility between grain  $i$  and  $j$  presuming that all grain boundaries share the same diffusion coefficient  $D_{gb}$  and grain boundary width  $\delta_{gb}$ .

The dissipation related to the phase fields,  $\Omega_\phi$  is taken as

$$\Omega_\phi(\boldsymbol{\pi}^{dis}) = \frac{1}{2} L(\boldsymbol{\phi}) \sum_i (\pi_i^{dis})^2 = \frac{1}{2} L(\boldsymbol{\phi}) \sum_i \left( \pi_i + \frac{\partial f}{\partial \phi_i} \right)^2 \quad (65)$$

for the kinetic coefficient,  $L(\boldsymbol{\phi})$  taken from [18] as

$$L(\boldsymbol{\phi}) = \frac{\sum_i \sum_{j \neq i} L_{ij} \phi_i^2 \phi_j^2}{\sum_i \sum_{j \neq i} \phi_i^2 \phi_j^2}. \quad (66)$$

In eq. (66)  $L_{ij}$  is chosen, as in [10], to be

$$L_{ij} = \frac{2mV_m}{3\alpha(\hat{x}_i - \hat{x}_j)^2} \frac{M_i + M_j}{2}, \quad (67)$$

for the mobilities  $M_k = \frac{D_k}{a_{1:k}^G}$ .

Dissipation originating from the crystal plasticity,  $\Omega_u$ , has in this work not been properly investigated. The reason for this is that a definition of hardening functions and internal variables was found too late to be properly derived. The model used in MOOSE uses the slip resistance as hardening variables thus looking at other works for inspiration: a natural format of the mechanical dissipation is found in [17], which, with the addition of the phase field interpolation,  $\sum_i h_i$ , would result in

$$\Omega_u(\boldsymbol{\phi}, c, \bar{M}_i, \bar{L}_i^p, \mathbf{K}_i, \boldsymbol{\kappa}_i) = \sum_i h_i \left[ \bar{M}_i : \bar{L}_i^p - \sum_\alpha \left( \frac{\partial f_i^{(p)}}{\partial s_i^\alpha} \right) \dot{s}_i^\alpha \right], \quad (68)$$

for some set of internal variables  $\boldsymbol{\kappa}_i$  and some hardening functions  $\mathbf{K}_i$ .

## 4 Governing Equations of the Simulation

With the use of eq. (42) and eq. (43) the state laws for the micro stress, chemical potential and the Cauchy stress becomes

$$\mu = \hat{\mu}; \quad \bar{\boldsymbol{\sigma}} = \sum_i \bar{\boldsymbol{\sigma}}_i = \sum_i h_i \left[ \bar{\mathbb{D}}_i : (\bar{\boldsymbol{\varepsilon}} - \bar{\boldsymbol{\varepsilon}}_i^{(p)} - \bar{\boldsymbol{\varepsilon}}_i^{(0)}) \right]; \quad \bar{\xi}_i = a_2^{int} \nabla \phi_i \quad (69)$$

In eq. (69) the chemical potential is the result of a diffusive constraint originating in the requirement that all phases are in equilibrium (c.f [10] and [19])

$$\mu_i = \frac{\partial G_i}{\partial x_i} = \frac{\partial G_j}{\partial x_j} = \hat{\mu} \quad (70)$$

Phase field parameters  $\phi_i$ , which are non conserved variables, will evolve according to eq. (46) which is calculated by the use of eq. (65) resulting in

$$\dot{\phi}_i = L(\boldsymbol{\phi}) \left( \pi_i + \frac{\partial f}{\partial \phi_i} \right). \quad (71)$$

Combining: the balance law of the micro forces while assuming that the external micro forces,  $\gamma_i = 0$ , eq. (32), and using the expression for the free energy density eq. (39), as well as adding an expression introducing nucleation of IMC into the model the following expression is obtained

$$\begin{aligned} \dot{\phi}_i = L(\phi) & \left[ \bar{\nabla} \cdot a_2^{int} \bar{\nabla} \phi_i - a_1^{int} \left( \phi_i^3 - \phi_i + 2\phi_i \sum_{j \neq i} a_3^{int} \phi_j^2 \right) \right. \\ & - \frac{2\phi_i}{\sum_k \phi_k^2} \left( (1 - h_i)(f_i^{(e)} + f_i^{(p)}) - \sum_{j \neq i} h_j(f_j^{(e)} + f_j^{(p)}) \right) \\ & \left. - \frac{2\phi_i}{\sum_k \phi_k^2} \left( (1 - h_i) \left( \frac{G_i}{V_m} - \frac{x_i}{V_m} \hat{\mu} \right) - \sum_{j \neq i} h_j \left( \frac{G_j}{V_m} - \frac{x_j}{V_m} \hat{\mu} \right) \right) \right] + \zeta(t, \bar{r}) \end{aligned} \quad (72)$$

In eq. (72) the nucleation term,  $\zeta(t, \bar{r})$ , is modelled in line with [22],

$$\zeta(t, \bar{r}) = \begin{cases} \rho \sqrt{\frac{2k_B T L}{\lambda^d \Delta t}}, \\ \text{for } 0 < t < 1 \text{ and } (h_{Cu} \cdot h_{Sn1} > 0.09 \text{ or } h_{Cu} \cdot h_{Sn2} > 0.09); \langle \rho_i \rangle = 0, \text{ and } \langle \rho_i \rho_j \rangle = \delta_{ij} \\ 0 \text{ else} \end{cases} \quad (73)$$

The nucleation term, eq. (73), involves the temperature,  $T$ , modelled as constant as the temperature variation is small for  $t < 1$ . Moreover  $\rho$  is a random number drawn from a distribution with the properties shown in the equation ( $\langle \cdot \rangle$  denoting expected mean),  $k_B$  is the Boltzmann constant,  $\lambda$  denotes the grid spacing and  $d$  denotes the number of spacial dimensions of the simulation,  $\Delta t$  is the time step length and lastly  $L$  is the mobility of the  $\eta$  phase.

Evolution of the concentration field will be in accordance with eq. (38) where the flux,  $\bar{J}$ , is replaced with the value obtained from eq. (47), providing

$$\dot{c} = \bar{\nabla} \cdot (M \bar{\nabla} \hat{\mu}). \quad (74)$$

MOOSE implements the problem using the residual expression belonging to each governing equation. Moreover introducing a more compact format of volume and surface integrals, let

$$\left( \psi_1, \psi_2 \right) \Leftrightarrow \int_V \psi_1 \psi_2 dV, \quad (75)$$

and

$$\left\langle \psi_1, \psi_2 \right\rangle \Leftrightarrow \int_{\partial V} \psi_1 \psi_2 dS. \quad (76)$$

The residual expressions are found by multiplying eq. (72) and (74) by a weight function,  $\psi$ , together with integration over the domain and with the use of the divergence theorem.

$$\mathbf{R}_i^\phi = \left( \frac{\partial \phi_i}{\partial t}, \psi \right) + \left( L \frac{\partial f}{\partial \phi_i}, \psi \right) + \left( \frac{\partial f_{int}}{\partial \bar{\nabla} \phi_i}, \bar{\nabla} L \psi \right) + \left( L \frac{\partial f_{int}}{\partial \bar{\nabla} \phi_i}, \bar{\nabla} \psi \right) + \left( \zeta, \psi \right) - \left\langle L \frac{\partial f_{int}}{\partial \bar{\nabla} \phi_i} \cdot \bar{n}, \psi \right\rangle = 0, \quad (77)$$

and

$$\mathbf{R}_c = \left( \frac{\partial c}{\partial t} \right) + \left( M \bar{\nabla} \hat{\mu} \cdot \bar{n}, \psi \right) - \left\langle M \bar{\nabla} \hat{\mu} \cdot \bar{n}, \psi \right\rangle = 0. \quad (78)$$

In both eq. (77) and (78) let  $\bar{n}$  be the outward normal of  $\partial V$ .

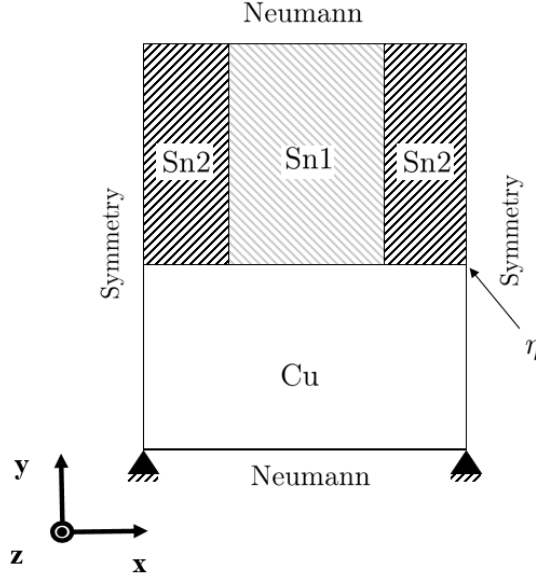


Figure 4: The domain used in the simulation showing the two tin grains on top of the copper and the interface where the intermetallic compound will nucleate.

## 5 Numerical Trials

Let the phases be denoted with the following subindices  $i = \{1, 2, 3, 4\} = \{\text{Cu}, \eta, \text{Sn1}, \text{Sn2}\}$ , where  $\eta$  denotes the IMC and where the number after Sn denotes which grain of tin that the phase corresponds to (for clarification see fig. (4)). In MOOSE a generated mesh with 8-noded hexahedron elements was used with a side length  $\Delta x = \Delta y = \Delta z = 16\text{nm}$  for a total domain size of  $80 \times 114 \times 1 = n_{el}^x \times n_{el}^y \times n_{el}^z$  where  $n_{el}$  denotes the number of elements in a dimension. The diffuse interface region width was taken to be  $5\Delta x$ .

Dirichlet boundary conditions were set to restrict displacement of the bottom boundary at the top and bottom of the domain.

Symmetric boundary conditions were set for the x-direction and z-direction.

Lastly Neumann boundary conditions were prescribed for the top and bottom of the domain so as to prohibit any flux over these boundaries of the domain.

The  $\eta$  is marked to the interface between the copper and tin where the nucleation is set to take place. All simulations were initially set so that a layer of Cu filled the bottom of the domain onto which two Sn grains were set. The two grains of the sides, i.e. phase  $i = \text{Sn2}$ , having been rotated using the Bunge-Euler angles  $\phi = 90^\circ, \psi = 90^\circ, \theta = 0^\circ$ , where the angles denotes rotation about the  $Z, X', Z''$  axis respectively. The governing equations were solved using a Preconditioned Jacobian Free Newton-Krylow (PJFNK in MOOSE) solver where the preconditioning is performed by PETSC. The time integration was performed using the L2StableDirk implemented in MOOSE together with an adaptive time step initially set to  $2E-2$  s.

### 5.1 Model Parameters

#### 5.1.1 Material Elastic and Plastic Parameters

The copper phase of the simulation as well as the IMC was modelled to be isotropically elastic with the constants seen in tab. (1).



Table 1: The elastic constants of the Cu and IMC phase

	Cu	$\eta$	Ref.
Young's modulus [GPa]	150	112.3	[7]
Poisson's ratio	0.35	0.31	[7]

Moreover the IMC is modelled to have a smaller volume than its constituents, and thus transformational strains are associated with the formation of IMC. The precise figure of this transformational strain is not clear but in this work

$$\bar{\bar{\epsilon}}^{(0)} = -0.003 \cdot \bar{\bar{I}}, \quad (79)$$

will be used which is in line with [10] where it is argued that strains of higher magnitude will cause stresses which are deemed nonphysical as they are larger than the yield stress of the  $\text{Cu}_6\text{Sn}_5$  which would then have to be modelled to be incorporating plasticity. The elastic constants used for tin is shown in tab. (2).

Table 2: The values used for the elastic stiffness tensor of the Tin. Values are taken from [5].

$\bar{\bar{\mathbb{D}}}$ [GPa]								
$D_{11}$	$D_{12}$	$D_{13}$	$D_{22}$	$D_{23}$	$D_{33}$	$D_{44}$	$D_{55}$	$D_{66}$
72.3	59.4	35.8	72.3	35.8	88.4	22.0	22.0	24.0

The parameter values used for the hardening of the crystal were the parameters seen in tab. (3) and (4).

Table 3: The parameters used for the crystal plasticity hardening taken from [14]. Note that crystal plane normals are given in Miller indices.

slip system family	$\tau_{sat}$ [MPa]
1 $\langle 100 \rangle \langle 001 \rangle$	11
2 $\langle 110 \rangle \langle 001 \rangle$	9
3 $\langle 100 \rangle \langle 010 \rangle$	11
4 $\langle 110 \rangle \langle \bar{1}\bar{1} \rangle$	9
5 $\langle 110 \rangle \langle \bar{1}\bar{1}0 \rangle$	10
6 $\langle 100 \rangle \langle 011 \rangle$	10
7 $\langle 001 \rangle \langle 010 \rangle$	10
8 $\langle 001 \rangle \langle 110 \rangle$	16
9 $\langle 011 \rangle \langle 0\bar{1}\bar{1} \rangle$	9
10 $\langle 211 \rangle \langle 0\bar{1}\bar{1} \rangle$	13

Table 4: Values used for the evolution laws of the slip resistance, the plastic slips, and the plastic energy  $f^{(p)}$ . (eq. (16), (14), and (60))

Parameter	values	Ref.
$c$	2	[14]
$m$	1/6	[4]
$h_0$	20 [MPa]	[4]
$\dot{\gamma}_0$	1E-3 [s <sup>-1</sup> ]	[26]
$Q$	1	-

Note that  $Q_i = Q$  in eq. (60) was used for both the  $Sn1$  and  $Sn2$  phase and that the parameters were used for all slip systems of the tin.

### 5.1.2 Temperature Dependent Parameters and Nucleation

To simulate a cooling phase of the simulation domain temperature dependent parameters (tab. (5)) were interpolated using

$$g_{temp}(t) = \frac{1 - \tanh\left(\frac{t - 11}{3}\right)}{2} \quad (80)$$

such that for a temperature dependent parameter  $f_{T-dep.}$  the value was calculated as

$$f_{T-dep.}(t) = f_{T-dep.}^{(25^\circ C)} - (f_{T-dep.}^{(25^\circ C)} - f_{T-dep.}^{(220^\circ C)})g_{temp}(t) \quad (81)$$

For the nucleation  $\lambda = 16\text{nm}$ ,  $T = 493\text{K}$  (approximated to be constant) and  $L = 2.7 \text{ m}^3\text{sJ}^{-1}$ .

Table 5: Constants used in the simulations where  $a_i^G$  have been obtained by curve fitting of parabolic functions. The starred quantities has not been taken from the stated reference.

	220°C			25°C			
	Cu	$\eta$	Sn	Cu	$\eta$	Sn	Ref.
$a_1^G[\text{Jm}^{-3}]$	1.7756E+10	2.4555E+11	2.3033E+10	6.2204E+09	2.4555E+10	2.5819E+11	[10]
$a_2^G[\text{Jm}^{-3}]$	-2.6351E+09	2.3251E+07	2.1422E+08	-1.2981E+09	-4.2905E+08	4.4002E+08	[10]
$a_3^G[\text{Jm}^{-3}]$	-1.1441E+09	-1.7646E+09	-1.6460E+09	-7.8834E+08	-1.1778E+09	-9.3708E+08	[10]
$\hat{x}$	0.02000	0.43510	1*	0.10569	0.41753	1*	[10]
$\hat{x}^{eq}$	0.02000	0.43510	0.99941*	0.10569	0.41753	0.99941	[10]
$D[\text{m}^2\text{s}^{-1}]$	1.0000E-20	3.1000E-14	1.0000E-13	2.8770E-36	6.5750E-19	2.4520E-17	[15],[16]
$\sigma^{int}[\text{Jm}^{-2}]$	0.5	0.5	0.5	0.5	0.5	0.5	[18]
$\delta_{gb}$	5.0000E-10	5.0000E-10	5.0000E-10	5.0000E-10	5.0000E-10	5.0000E-10	-

Moreover the kinetic coefficient related to the phase field dissipation eq. (66) is taken to be  $2.7 \text{ m}^3\text{sJ}^{-1}$  constant.

## 6 Result and Discussion - Read remark

### Author's remark

Post performing all simulations it was noted that the slip systems file used was erroneous. The slip plane normals seen in tab. (6) was not put in right. The slip plane normals should be put in using the miller indices as they are already giving the plane normals.

All images are taken at approximate times as the timestep was set to be adaptive. In figs. (5) to (24) going left to right: The first figure shows the accumulated slips (c.f eq. (20)) in both tin grains. The second figure shows the value of the interpolation function of the  $\eta$  phase, i.e. the amount of IMC, and boundaries of the tin grains and the copper are shown in black. The rightmost figure shows the von Mises stress given in MPa field in the tin grains. Below each figure the Bunge-Euler angles used to rotate the middle tin grains are shown as well as the approximate time of the snapshot. The rotation angles of the outer tin grains is left out as they all have the same alignment throughout all simulations.

In fig. (25) the accumulated slips ( $\gamma_{Sn2}^{tot}$ ) is shown for all the simulations taken approximately 5 s into the simulation.

### 6.1 Simulation where $S_{n1}$ is rotated using $\phi = 90^\circ, \psi = 30^\circ, \theta = 0^\circ$

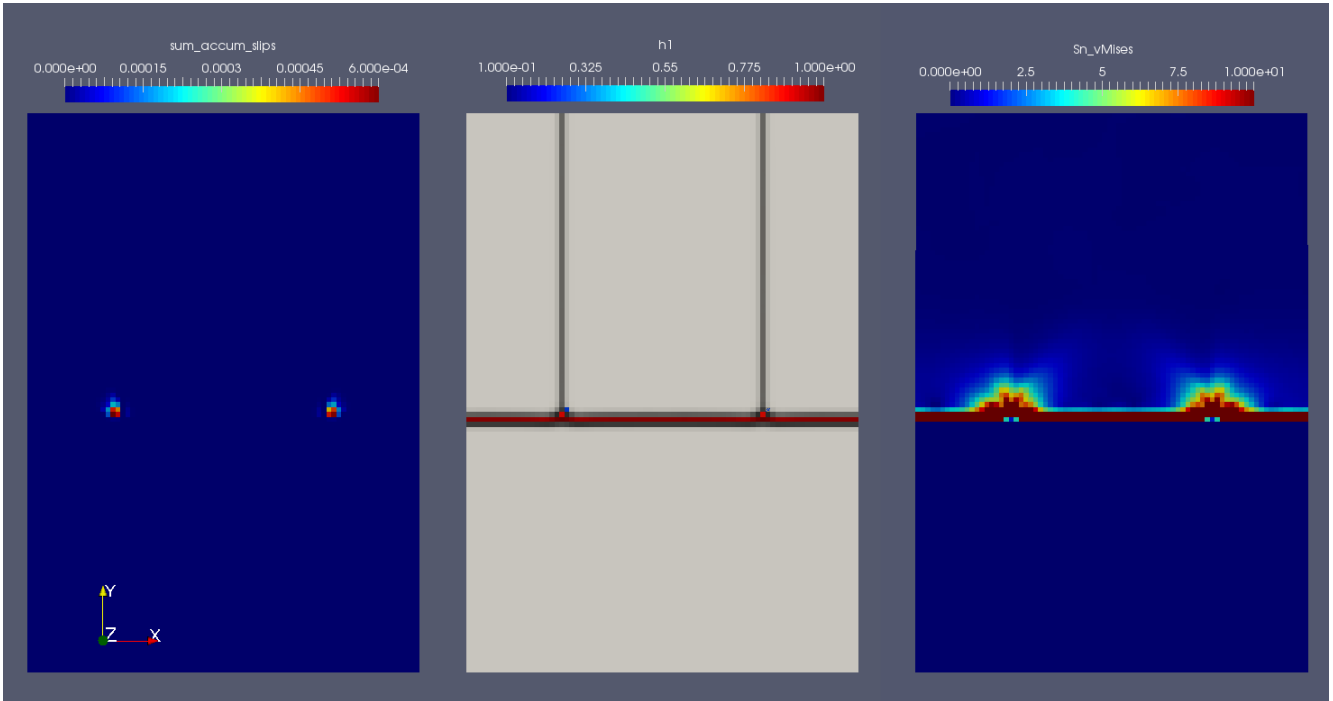


Figure 5:  $\phi = 90^\circ, \psi = 30^\circ, \theta = 0^\circ$ . The figure shows the accumulated plastic slips (left). The IMC (middle), and von Mises stress in both tin grains (right). The snapshot is taken at approximately 0.5 s into the simulation.

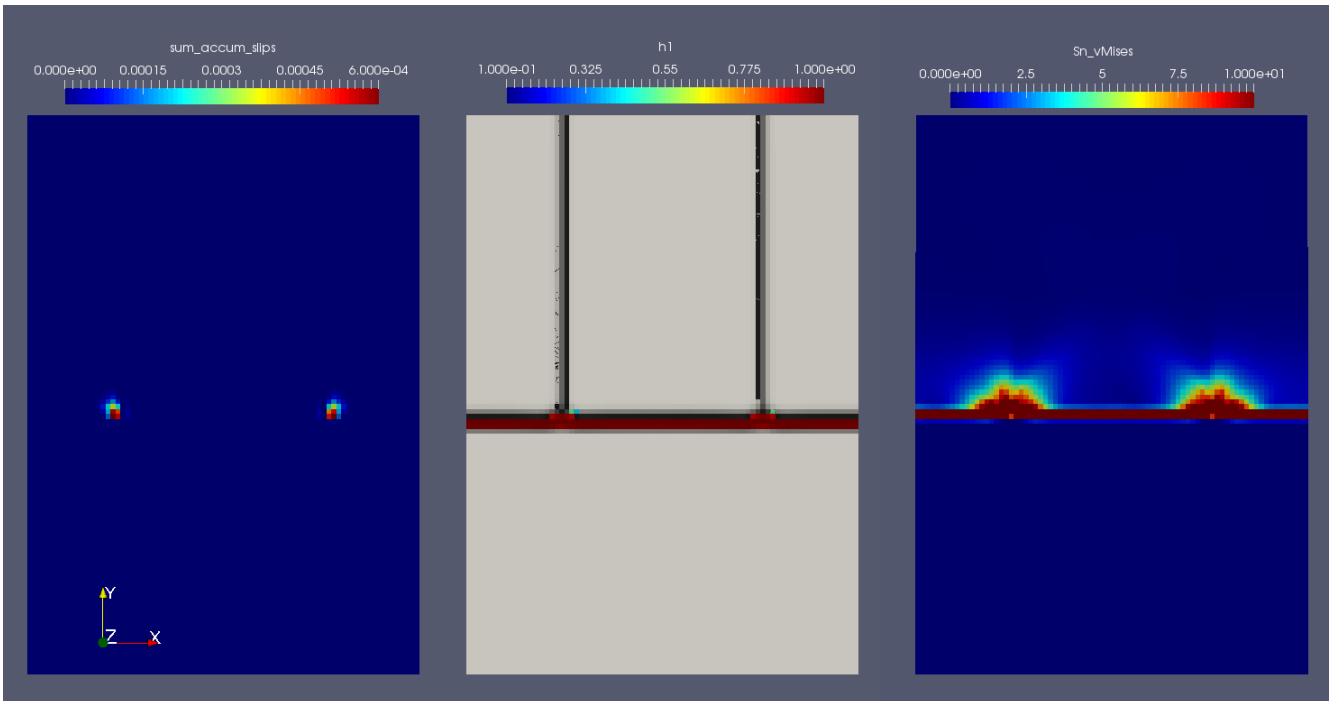


Figure 6:  $\phi = 90^\circ, \psi = 30^\circ, \theta = 0^\circ$ . The figure shows the accumulated plastic slips (left). The IMC (middle), and von Mises stress in both tin grains (right). The snapshot is taken at approximately 1 s into the simulation.

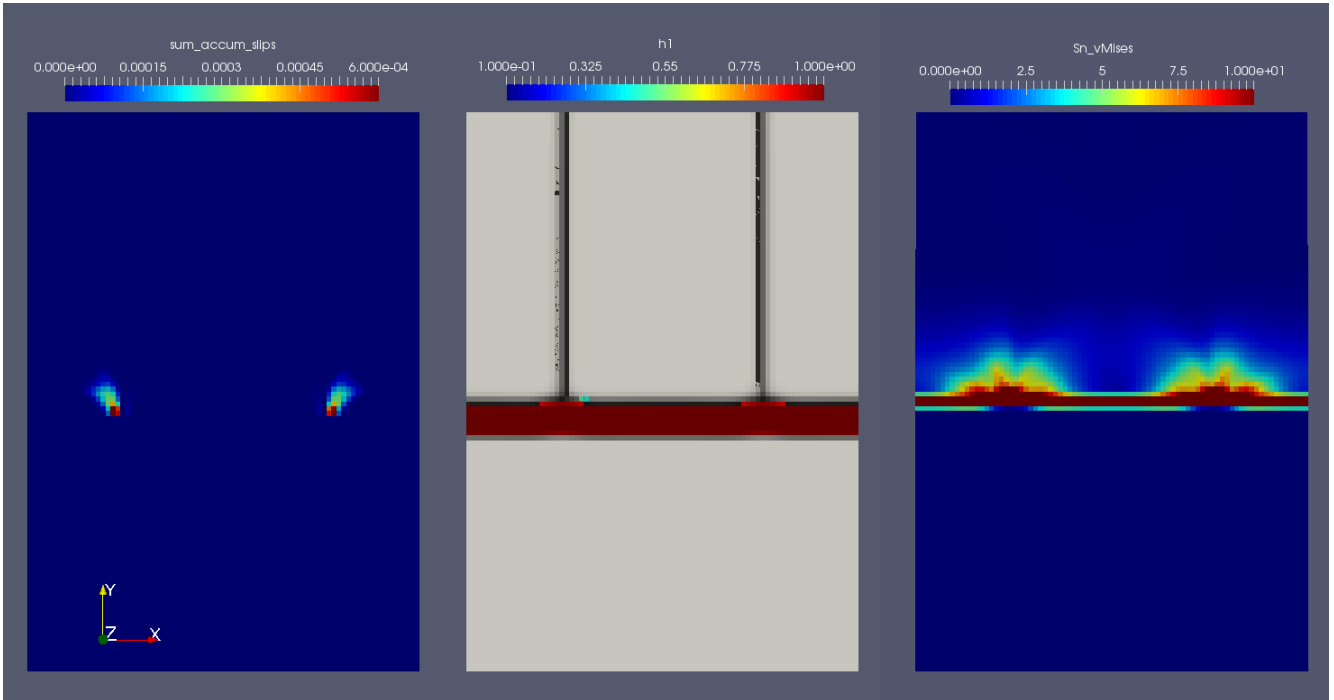


Figure 7:  $\phi = 90^\circ, \psi = 30^\circ, \theta = 0^\circ$ . The figure shows the accumulated plastic slips (left). The IMC (middle), and von Mises stress in both tin grains (right). The snapshot is taken at approximately 5 s into the simulation.

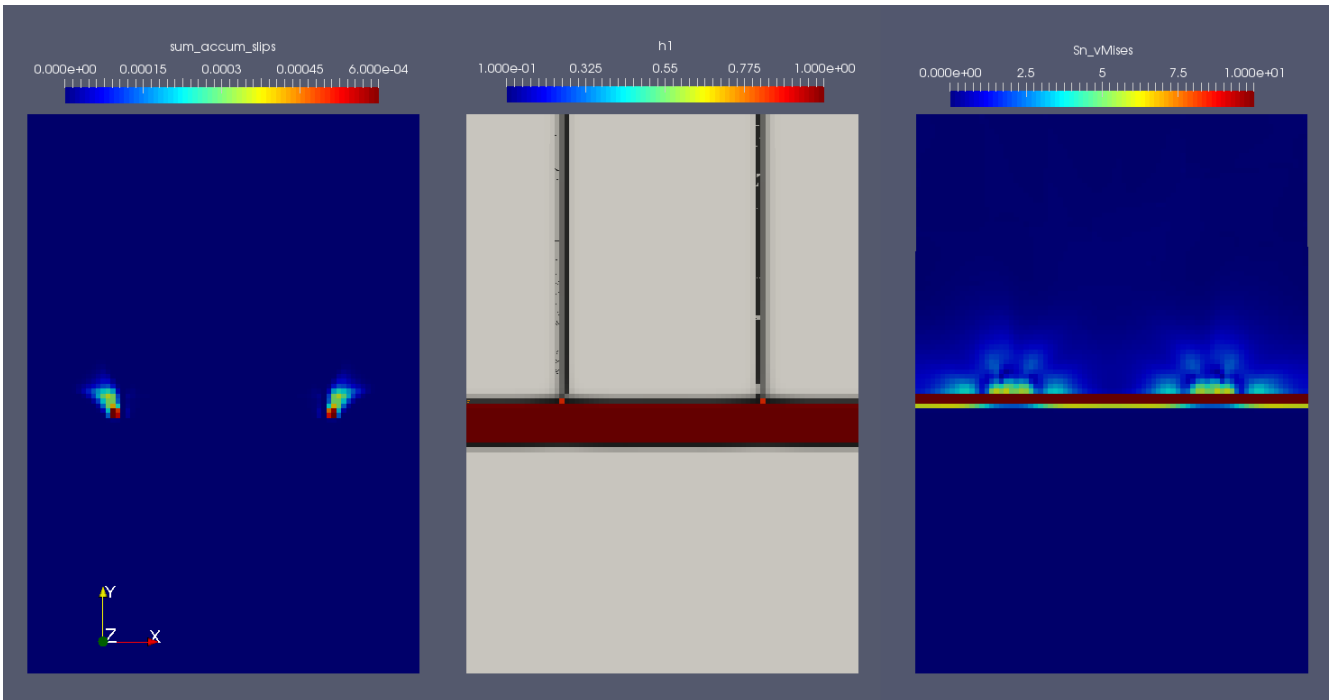


Figure 8:  $\phi = 90^\circ, \psi = 30^\circ, \theta = 0^\circ$ . The figure shows the accumulated plastic slips (left). The IMC (middle), and von Mises stress in both tin grains (right). The snapshot is taken at approximately 10 s into the simulation.

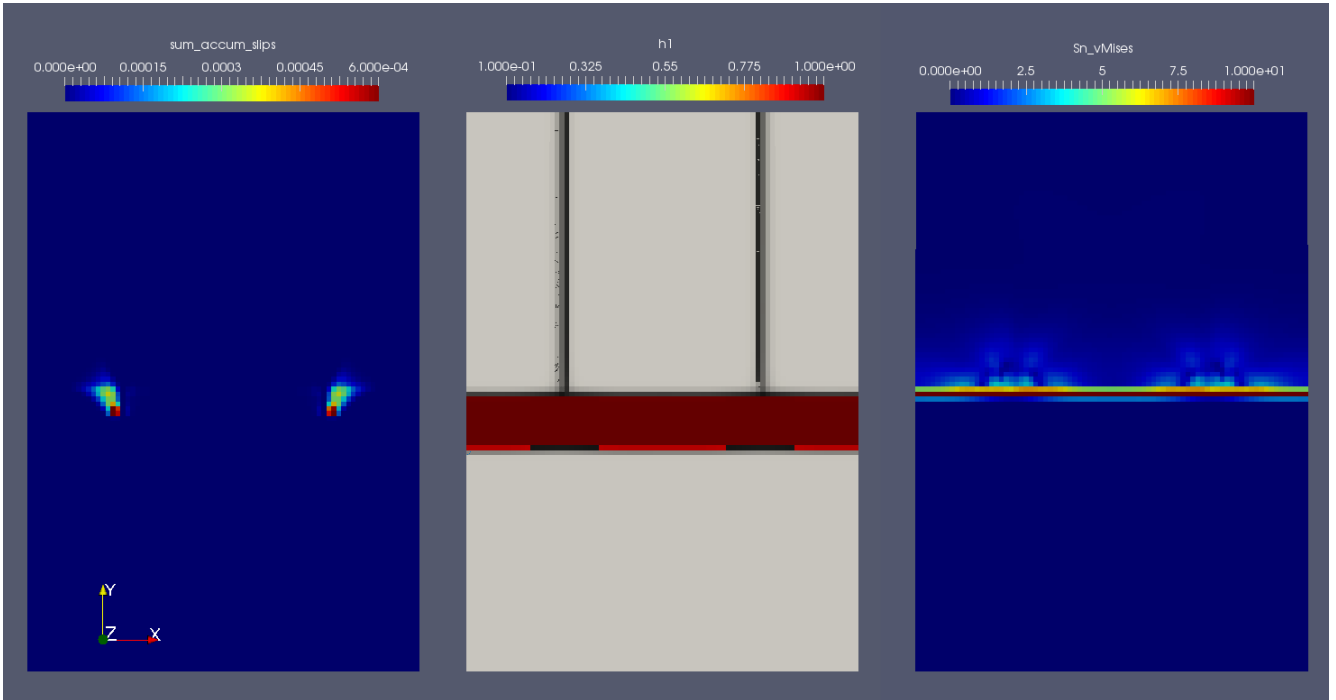


Figure 9:  $\phi = 90^\circ, \psi = 30^\circ, \theta = 0^\circ$ . The figure shows the accumulated plastic slips (left). The IMC (middle), and von Mises stress in both tin grains (right). The snapshot is taken at approximately 20 s into the simulation.

## 6.2 Simulation where $Sn1$ is rotated using $\phi = 90^\circ, \psi = 30^\circ, \theta = 345^\circ$

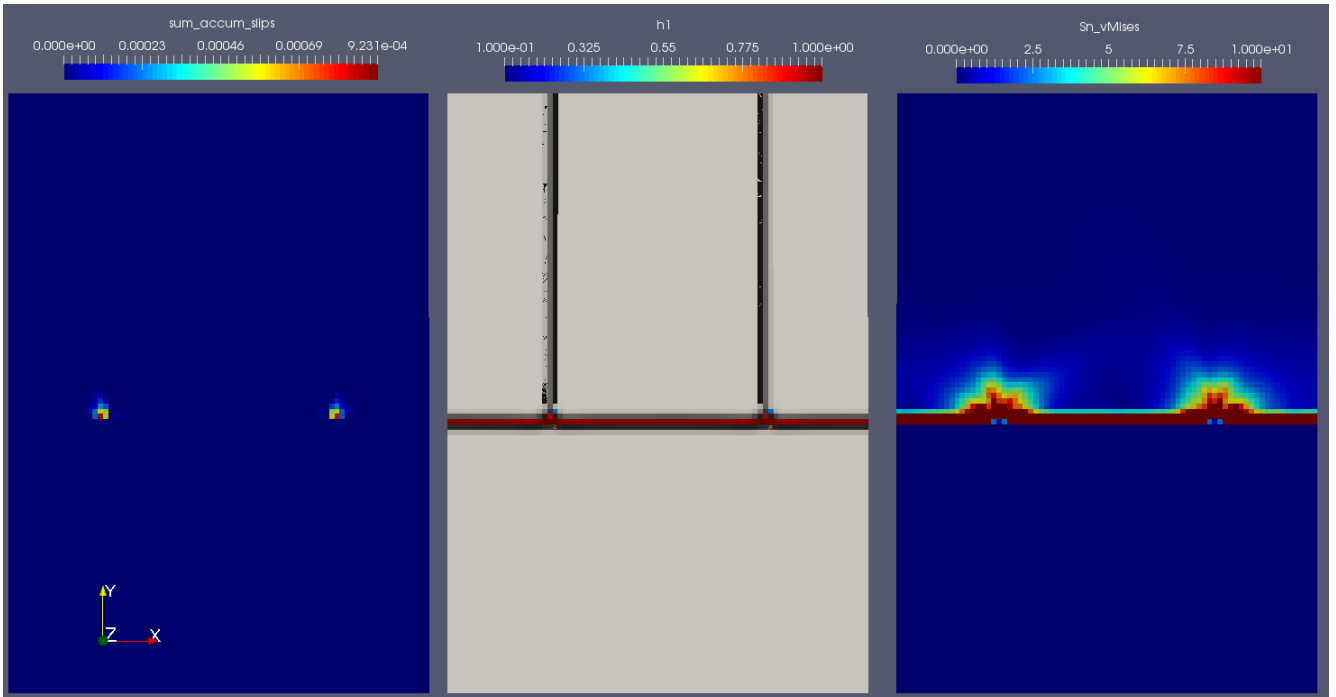


Figure 10:  $\phi = 90^\circ, \psi = 30^\circ, \theta = 345^\circ$ . The figure shows the accumulated plastic slips (left). The IMC (middle), and von Mises stress in both tin grains (right). The snapshot is taken at approximately 0.5 s into the simulation. Now both the  $\bar{a}$ , and  $\bar{b}$  axis of the middle grain is out of the  $\bar{x}\bar{z}$ -plane.

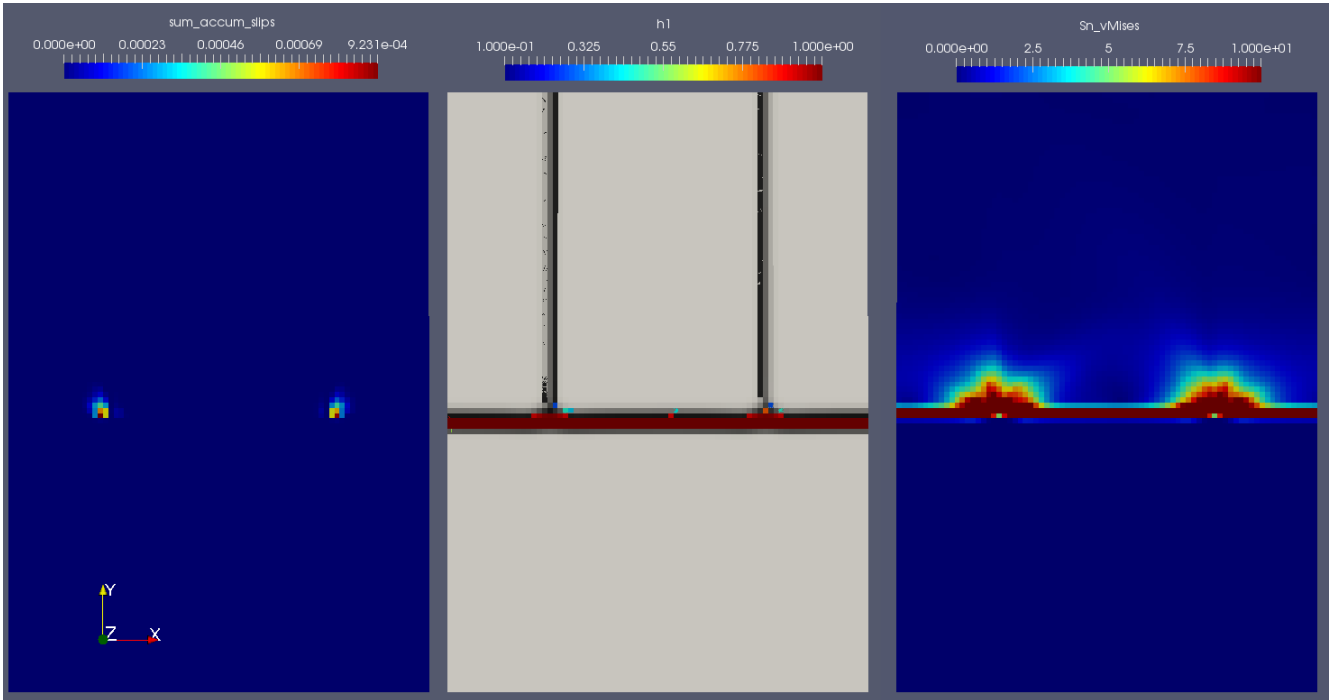


Figure 11:  $\phi = 90^\circ, \psi = 30^\circ, \theta = 345^\circ$ . The figure shows the accumulated plastic slips (left). The IMC (middle), and von Mises stress in both tin grains (right). The snapshot is taken at approximately 1 s into the simulation. Now both the  $\bar{a}$ , and  $\bar{b}$  axis of the middle grain is out of the  $\bar{x}\bar{z}$ -plane.

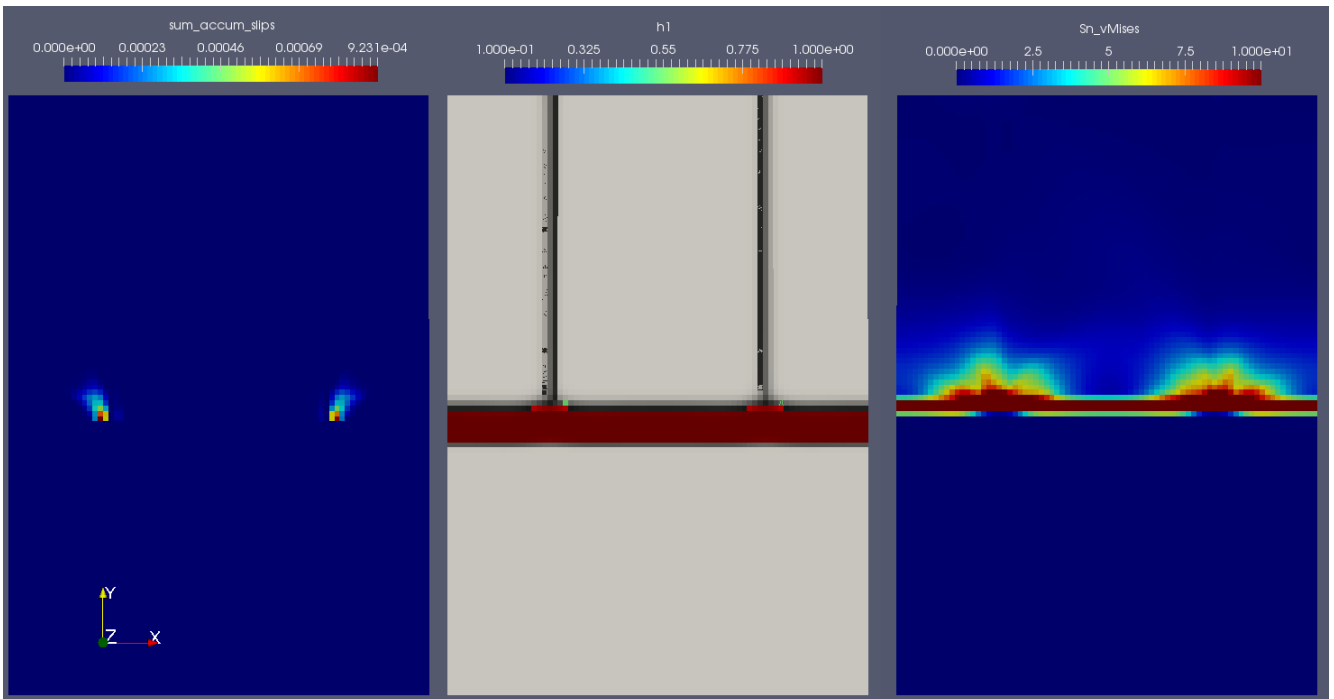


Figure 12:  $\phi = 90^\circ, \psi = 30^\circ, \theta = 345^\circ$ . The figure shows the accumulated plastic slips (left). The IMC (middle), and von Mises stress in both tin grains (right). The snapshot is taken at approximately 5 s into the simulation. Now both the  $\bar{a}$ , and  $\bar{b}$  axis of the middle grain is out of the  $\bar{x}\bar{z}$ -plane.

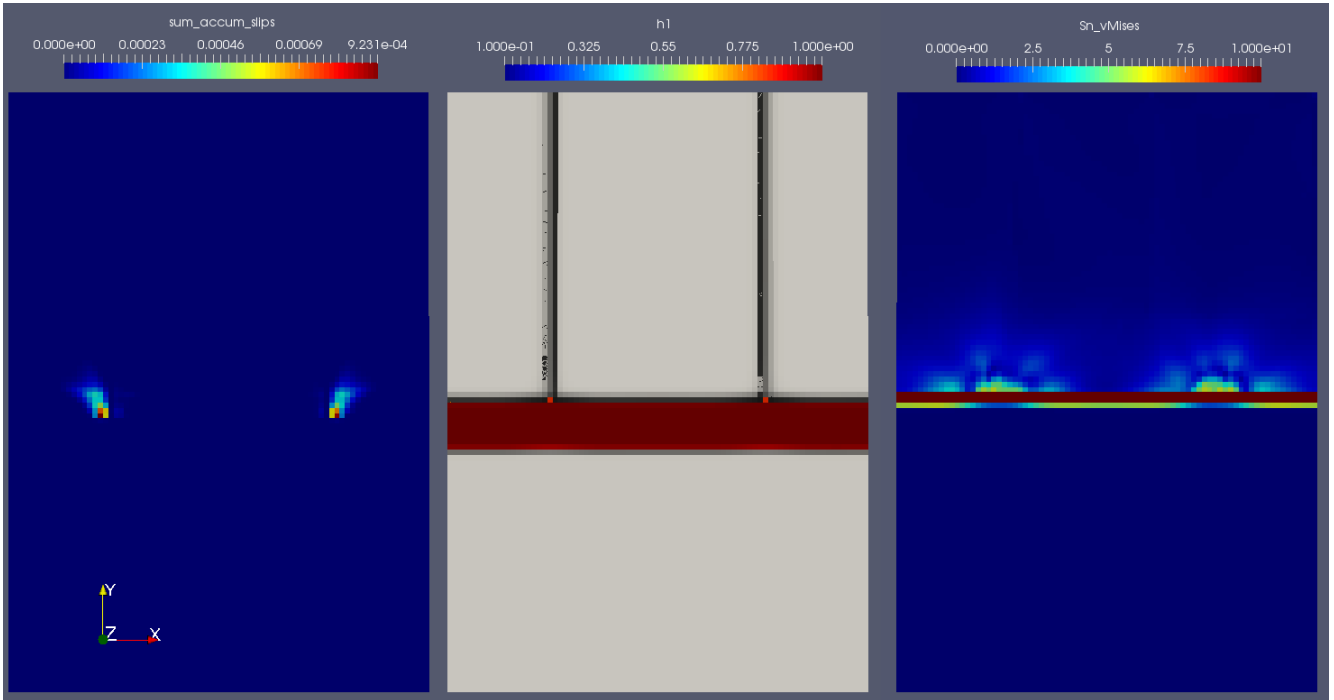


Figure 13:  $\phi = 90^\circ, \psi = 30^\circ, \theta = 345^\circ$ . The figure shows the accumulated plastic slips (left). The IMC (middle), and von Mises stress in both tin grains (right). The snapshot is taken at approximately 10 s into the simulation. Now both the  $\bar{a}$ , and  $\bar{b}$  axis of the middle grain is out of the  $\bar{x}\bar{z}$ -plane.

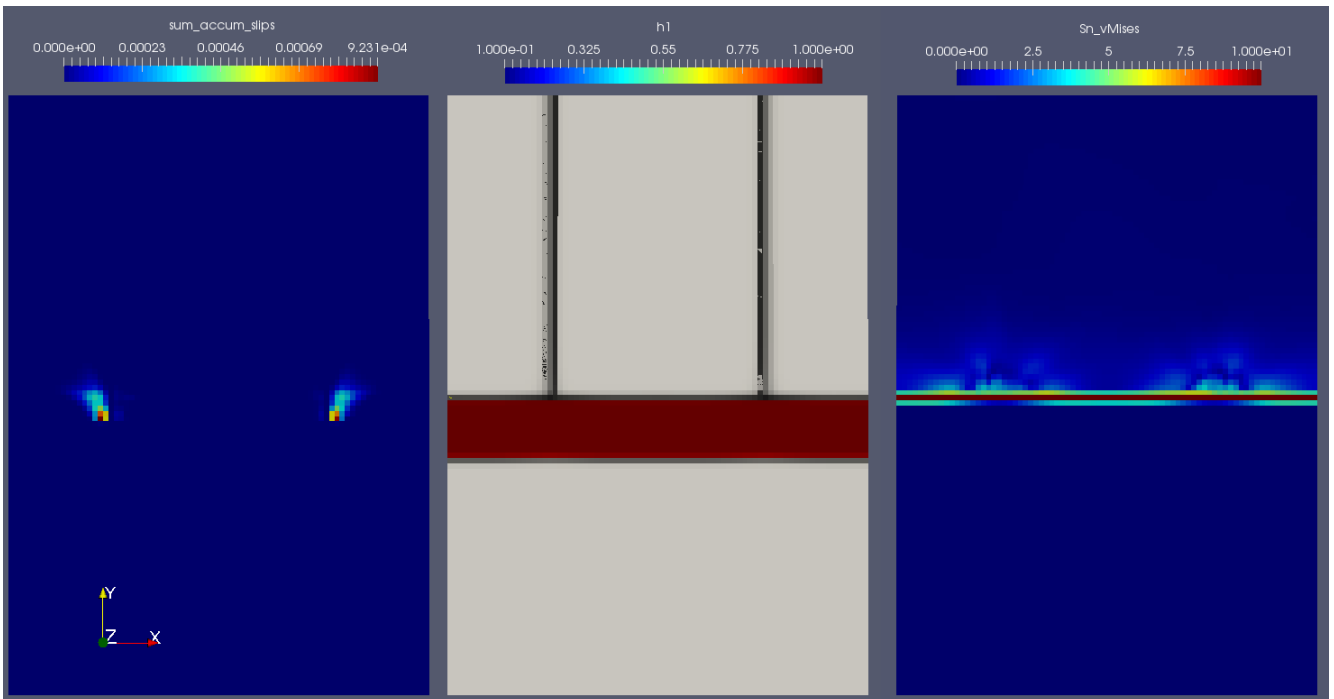


Figure 14:  $\phi = 90^\circ, \psi = 30^\circ, \theta = 345^\circ$ . The figure shows the accumulated plastic slips (left). The IMC (middle), and von Mises stress in both tin grains (right). The snapshot is taken at approximately 20 s into the simulation. Now both the  $\bar{a}$ , and  $\bar{b}$  axis of the middle grain is out of the  $\bar{x}\bar{z}$ -plane.

### 6.3 Simulation where $Sn1$ is rotated using $\phi = 90^\circ, \psi = 30^\circ, \theta = 315^\circ$

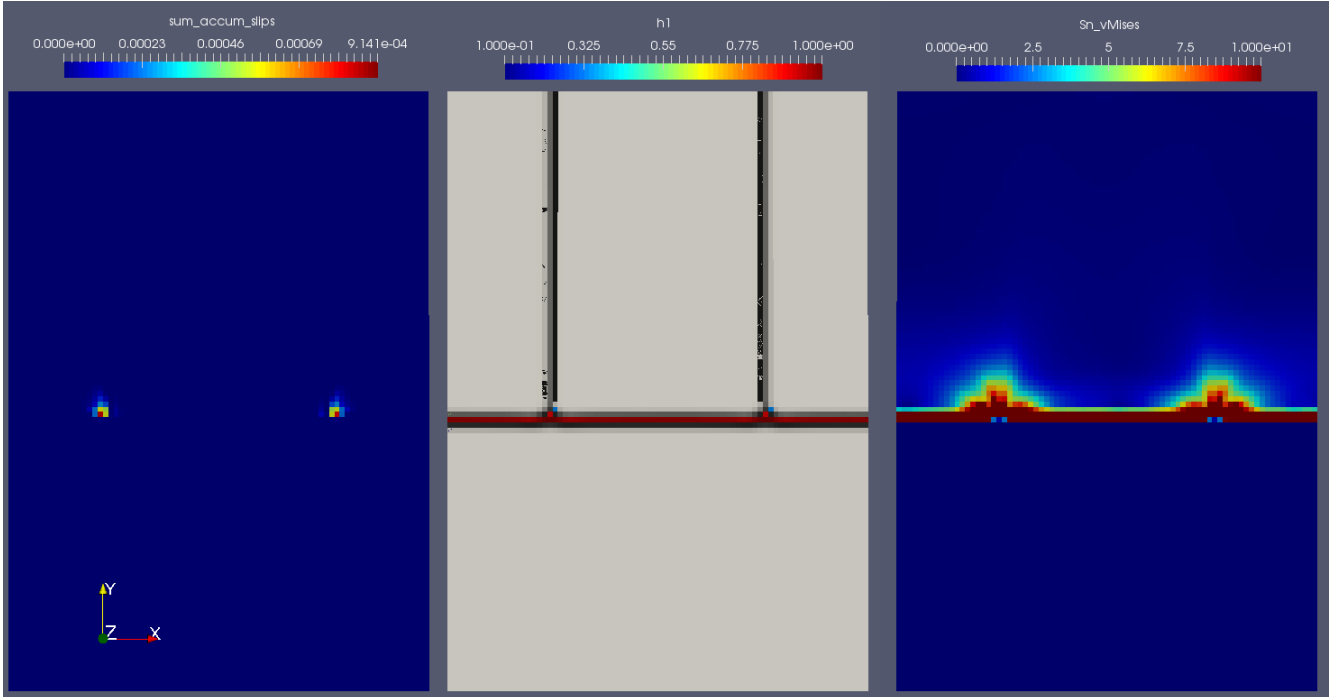


Figure 15:  $\phi = 90^\circ, \psi = 30^\circ, \theta = 315^\circ$ . The figure shows the accumulated plastic slips (left). The IMC (middle), and von Mises stress in both tin grains (right). The snapshot is taken at approximately 0.5 s into the simulation. Now both the  $\bar{a}$ , and  $\bar{b}$  axis of the middle grain is out of the  $\bar{x}\bar{z}$ -plane.

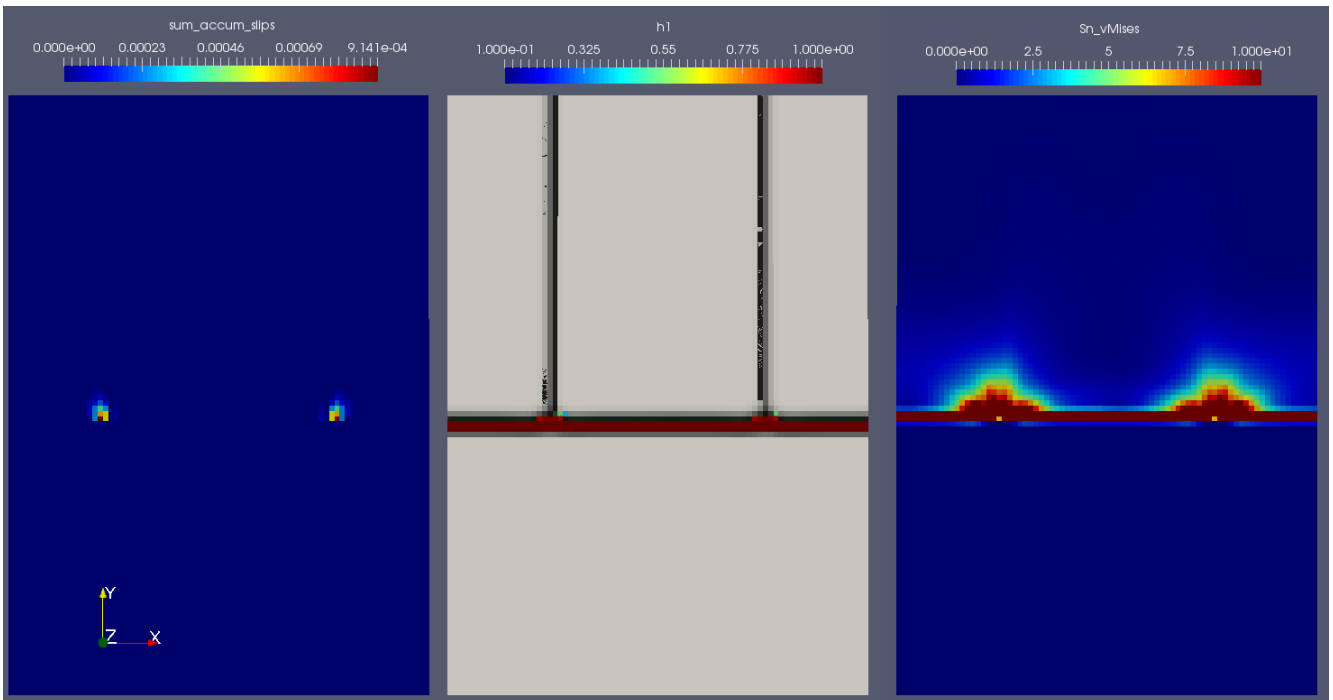


Figure 16:  $\phi = 90^\circ, \psi = 30^\circ, \theta = 315^\circ$ . The figure shows the accumulated plastic slips (left). The IMC (middle), and von Mises stress in both tin grains (right). The snapshot is taken at approximately 1 s into the simulation. Now both the  $\bar{a}$ , and  $\bar{b}$  axis of the middle grain is out of the  $\bar{x}\bar{z}$ -plane.



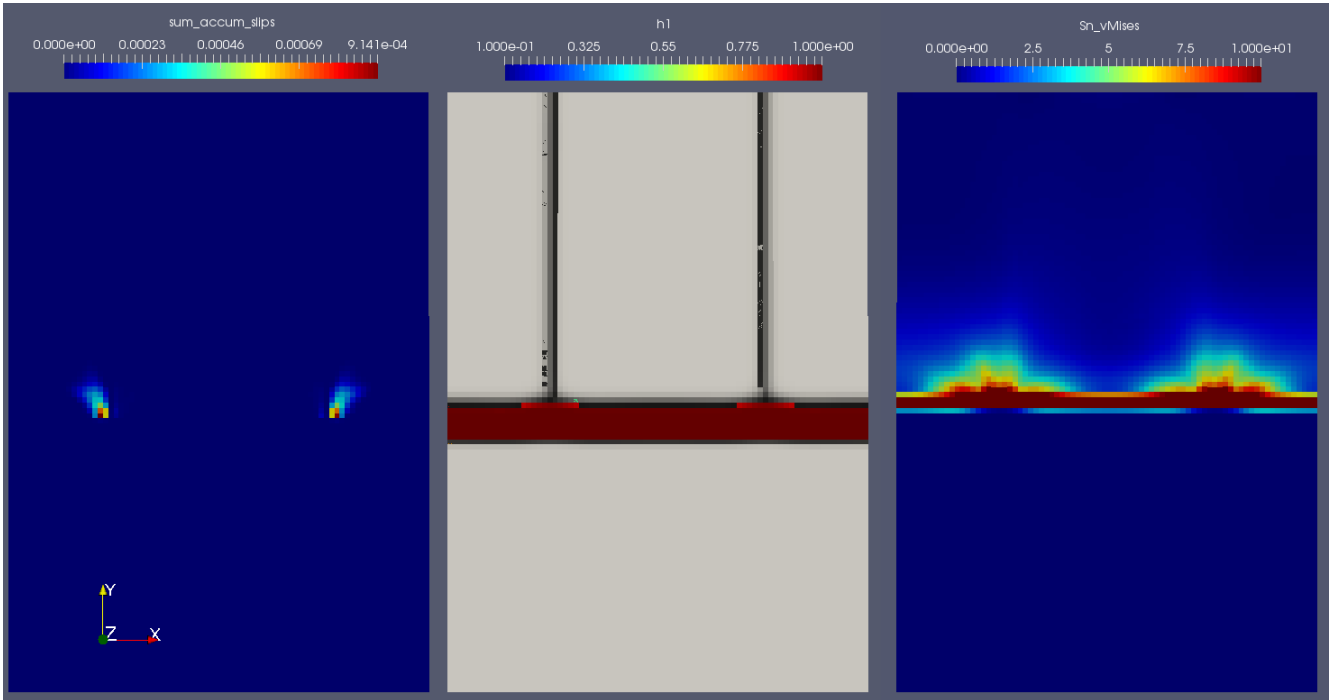


Figure 17:  $\phi = 90^\circ, \psi = 30^\circ, \theta = 315^\circ$ . The figure shows the accumulated plastic slips (left). The IMC (middle), and von Mises stress in both tin grains (right). The snapshot is taken at approximately 5 s into the simulation. Now both the  $\bar{a}$ , and  $\bar{b}$  axis of the middle grain is out of the  $\bar{x}\bar{z}$ -plane.

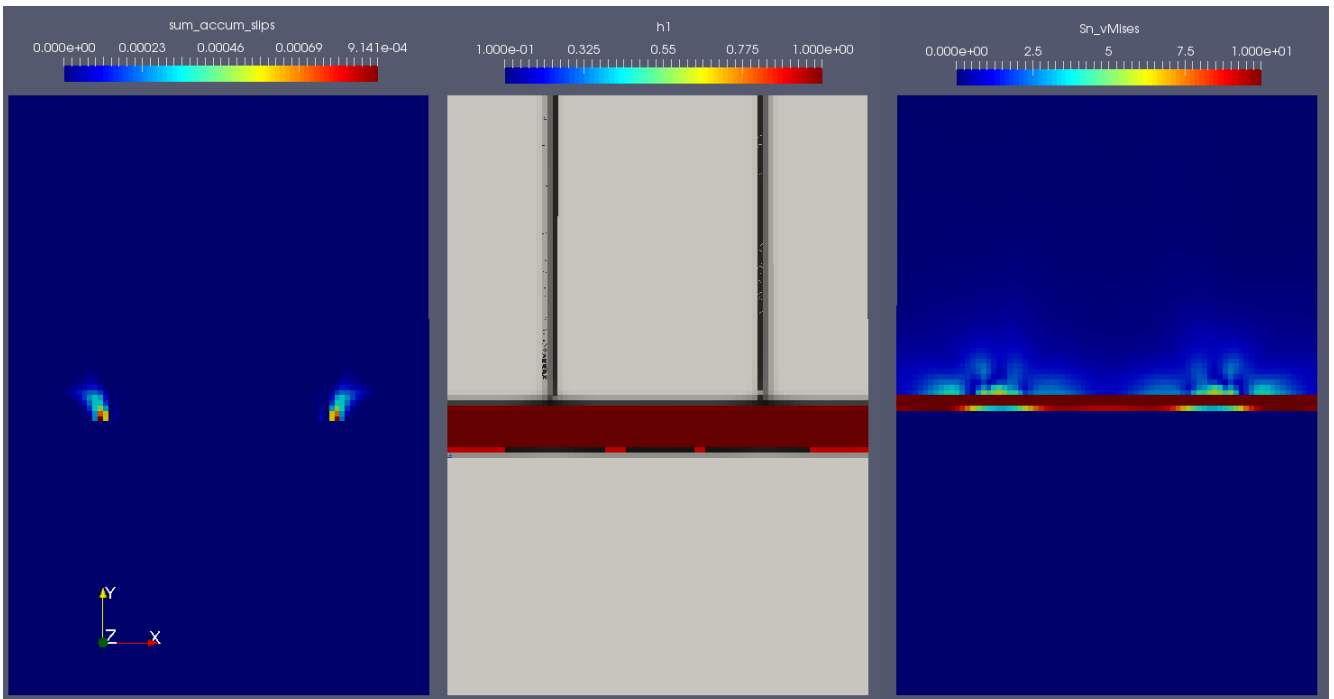


Figure 18:  $\phi = 90^\circ, \psi = 30^\circ, \theta = 315^\circ$ . The figure shows the accumulated plastic slips (left). The IMC (middle), and von Mises stress in both tin grains (right). The snapshot is taken at approximately 10 s into the simulation. Now both the  $\bar{a}$ , and  $\bar{b}$  axis of the middle grain is out of the  $\bar{x}\bar{z}$ -plane.

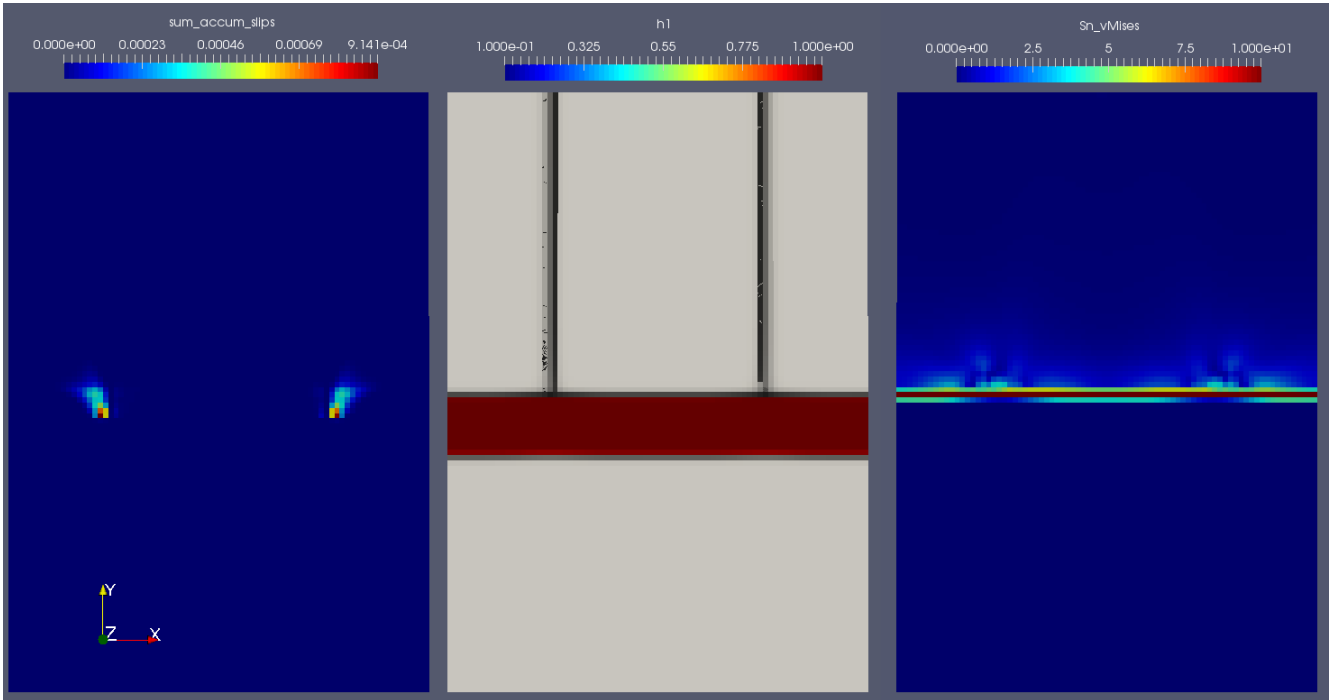


Figure 19:  $\phi = 90^\circ, \psi = 30^\circ, \theta = 315^\circ$ . The figure shows the accumulated plastic slips (left). The IMC (middle), and von Mises stress in both tin grains (right). The snapshot is taken at approximately 20 s into the simulation. Now both the  $\bar{a}$ , and  $\bar{b}$  axis of the middle grain is out of the  $\bar{x}\bar{z}$ -plane.

#### 6.4 Simulation where $Sn1$ is rotated using $\phi = 90^\circ, \psi = 75^\circ, \theta = 0^\circ$

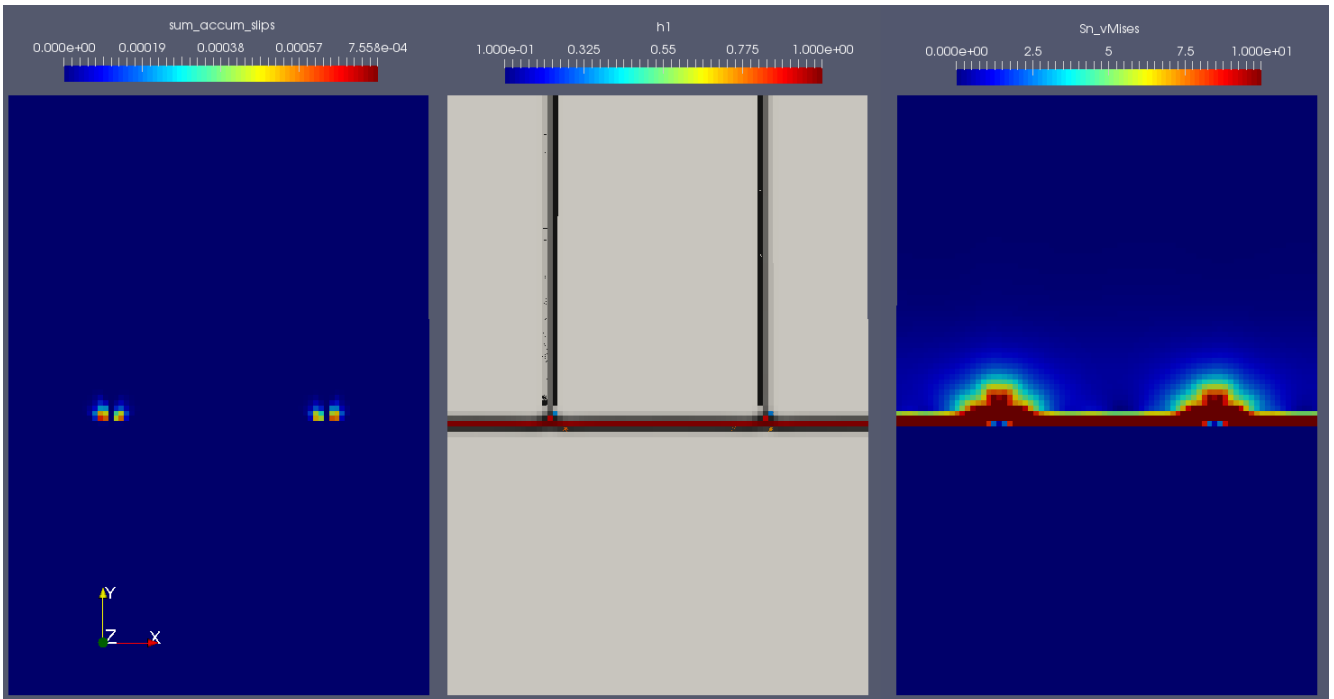


Figure 20:  $\phi = 90^\circ, \psi = 75^\circ, \theta = 0^\circ$ . The figure shows the accumulated plastic slips (left). The IMC (middle), and von Mises stress in both tin grains (right). The snapshot is taken at approximately 0.5 s into the simulation.

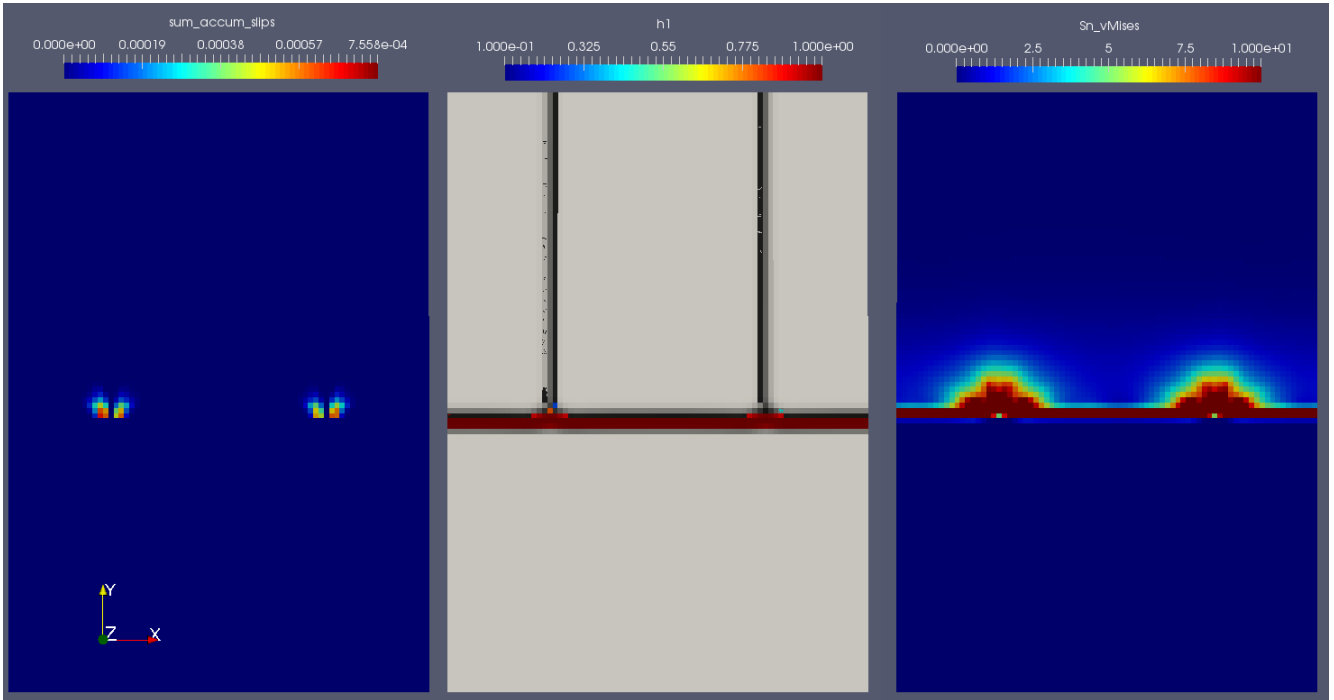


Figure 21:  $\phi = 90^\circ, \psi = 75^\circ, \theta = 0^\circ$ . The figure shows the accumulated plastic slips (left). The IMC (middle), and von Mises stress in both tin grains (right). The snapshot is taken at approximately 1 s into the simulation.

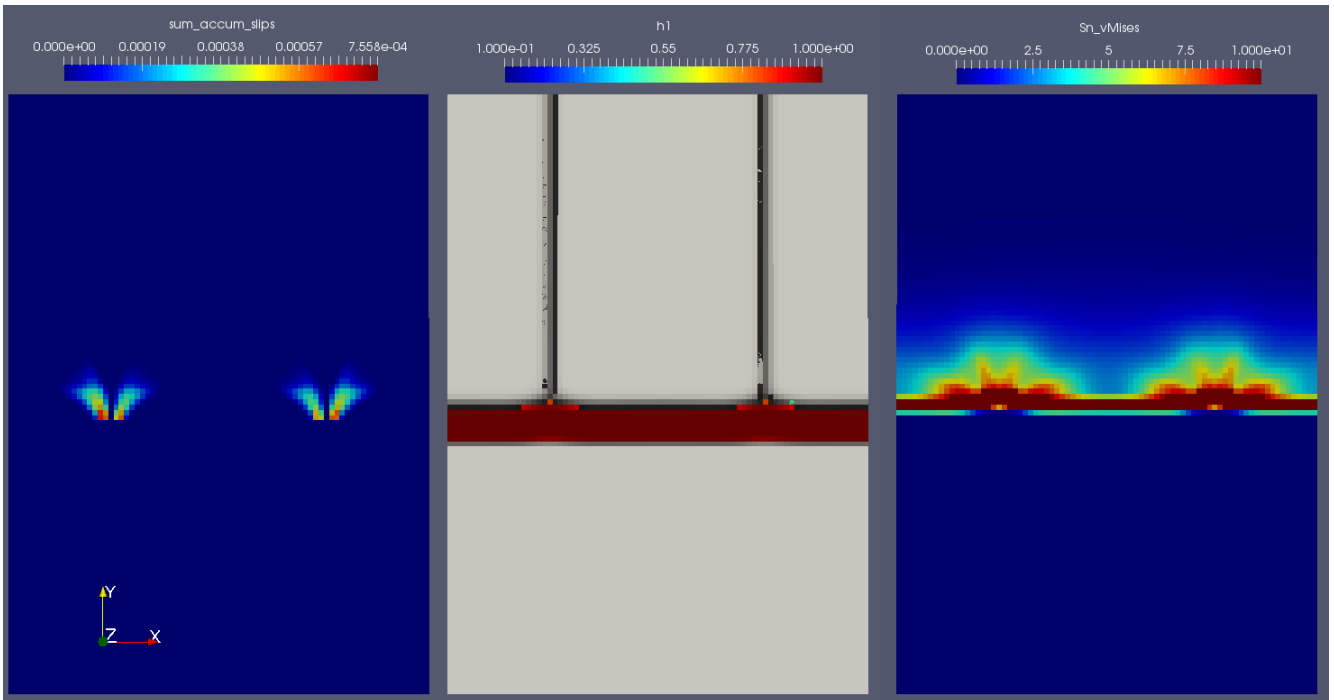


Figure 22:  $\phi = 90^\circ, \psi = 75^\circ, \theta = 0^\circ$ . The figure shows the accumulated plastic slips (left). The IMC (middle), and von Mises stress in both tin grains (right). The snapshot is taken at approximately 5 s into the simulation.

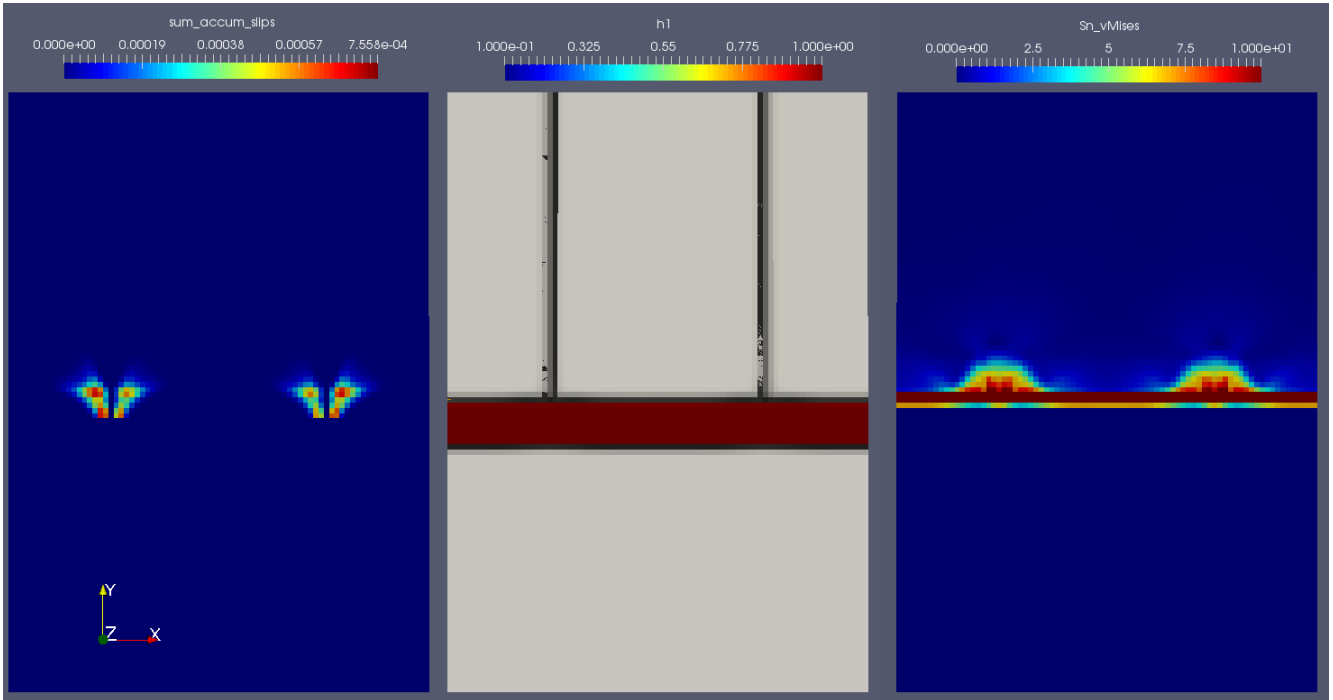


Figure 23:  $\phi = 90^\circ, \psi = 75^\circ, \theta = 0^\circ$ . The figure shows the accumulated plastic slips (left). The IMC (middle), and von Mises stress in both tin grains (right). The snapshot is taken at approximately 10 s into the simulation.

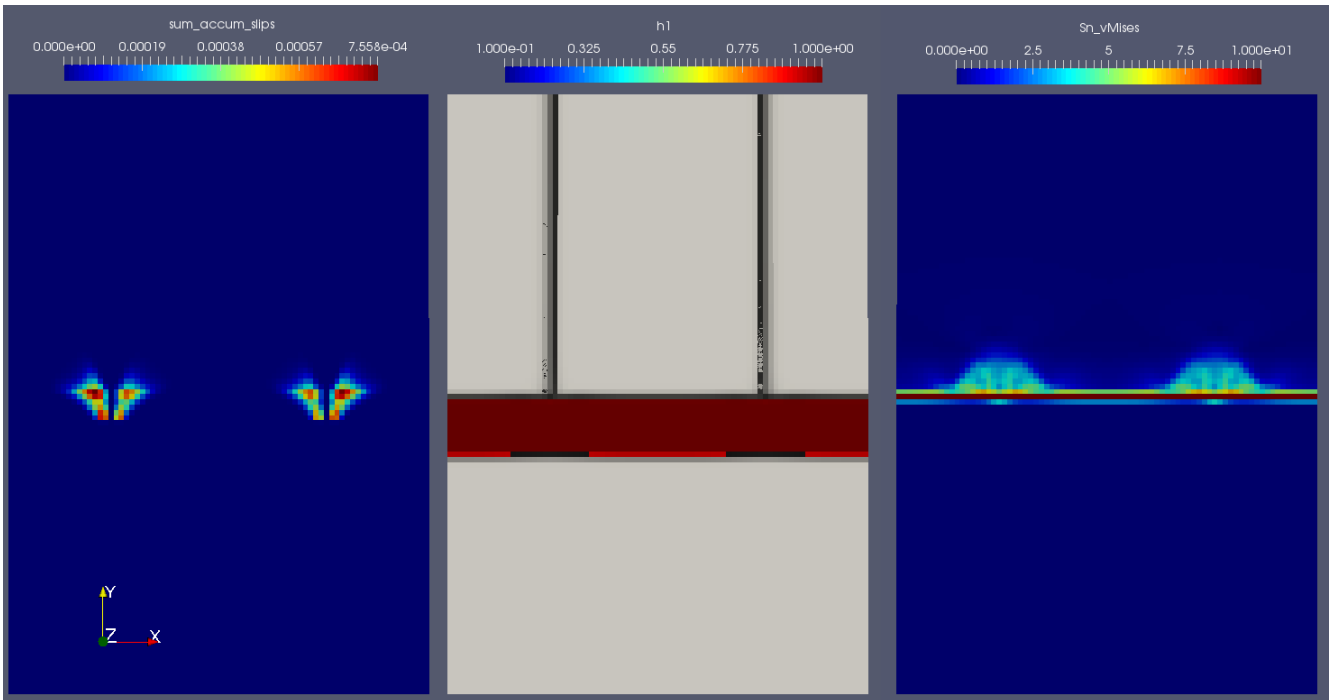


Figure 24:  $\phi = 90^\circ, \psi = 75^\circ, \theta = 0^\circ$ . The figure shows the accumulated plastic slips (left). The IMC (middle), and von Mises stress in both tin grains (right). The snapshot is taken at approximately 20 s into the simulation.

## 6.5 Accumulated Plastic Slips of the Middle Tin Grain

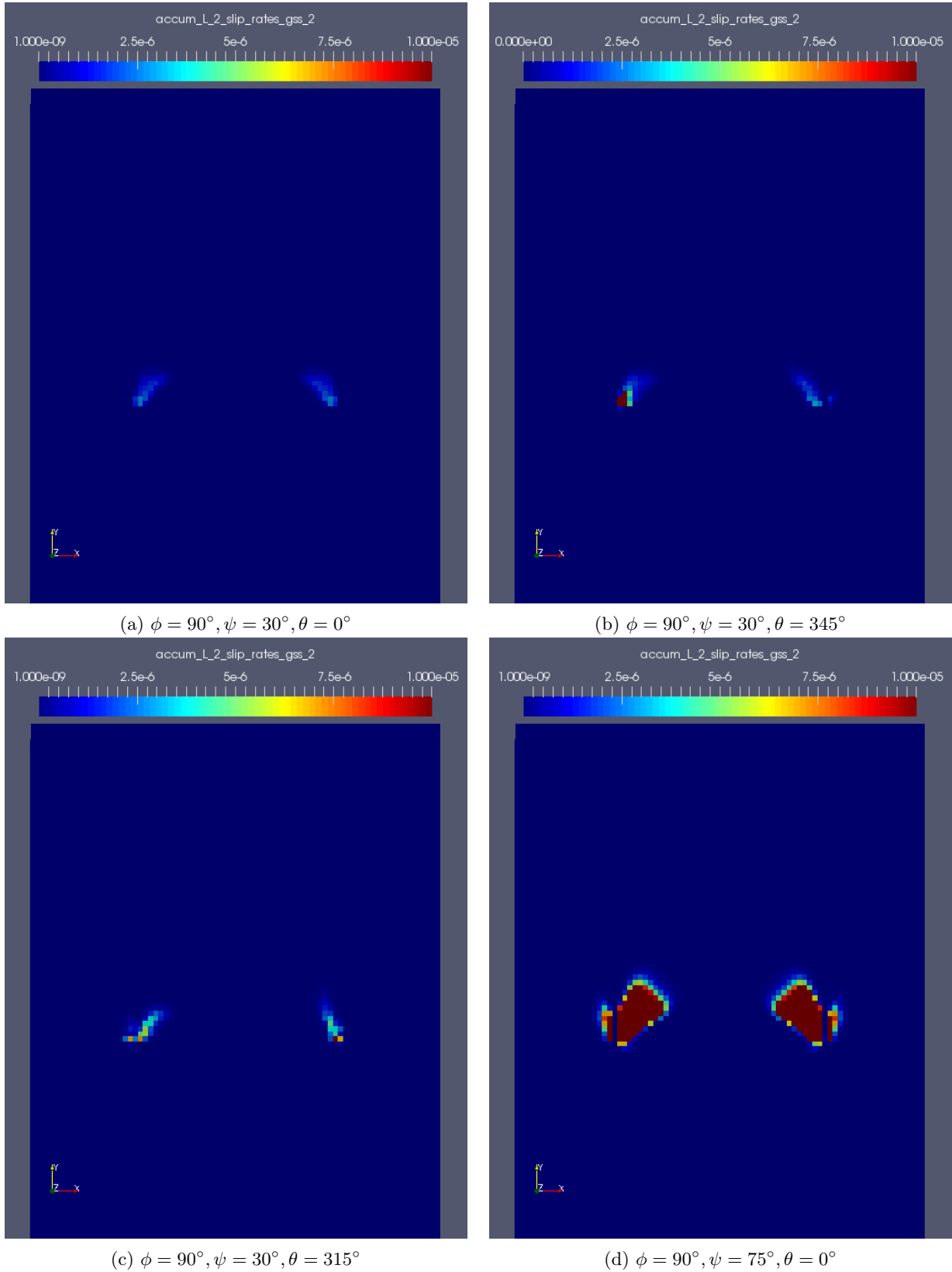


Figure 25: Comparison of the accumulated slips ( $\gamma_{Sn2}^{tot}$ ) that has developed in the middle tin grain. All snapshots are taken at approximately 5 s. The respective Bunge-Euler angles of each simulation is shown below each figure.

## 6.6 Discussion

Looking at the growth of the IMC, which is denoted as the variable,  $h_1$  in the middle figure of the simulation results, it seems to favour the triple junctions between the middle and side grains of the tin and the copper as a place to nucleate. This can be seen in the beginning of all simulations (the middle figure in figs. (5), (6), (10), (11), (15), (16), and (20), (21)). Since the nucleation in all simulations is the same it is not strange that they all have IMC starting to form at the same place, however it is not evident why this takes place in the triple junction. There is no clear cause to this: it might be that the IMC naturally grows easier in these areas as an effect of the material properties. Another possible, though unlikely, cause is that the Boolean expression governing the nucleation gives rise to a more probable region where both expressions are true. Nevertheless it is not deemed as a flaw in the simulation as the nature of the IMC nucleation is unclear and the focus of this work is to look at stresses arising from the IMC forming. Wherever it forms.

Continuing to look at the formation of the IMC it does not seem to have a preferred diffusion path. It forms fairly uniform across the interface both towards the tin and towards the copper. As seen at the final snapshots (figs. (9),(24),(14), and (19)) the small areas at the triple junctions disappears into the bulk of the IMC. The compound forms its own layer between the copper and tin having high on horizontal borders to the other metals. This is to be expected as the concentration field is driven by the divergence of the mobility and the gradient of the chemical potential. As the whole area above the IMC consists of tin, the concentration should evolve similarly across the entire interface as no dependence on crystal orientation is present neither for the mobility's (eq. (63)), nor for the chemical potentials  $\hat{\mu}$ . The diffusion in itself should be driven by the opportunity for the copper and tin to reach a lower potential if they instead form the IMC [10]. The phase fields should follow the concentration field as they depend on the molar fractions of each phase, which in turn are interpolated to form the concentration field. The interface between the copper and the IMC will develop analogously.

Moving on to the areas where plasticity is largest for the tin: it is natural that elements close to where the IMC grows the most should experience the largest von Mises stresses and thus also obtain larger slips since the resolved shear stress is expected to be larger in these areas. Of course the alignment of the crystal comes in to play as only deviatoric stresses are projected onto the Schmidt tensor and thus for alignments where the crystal experience more hydro-static stress the resolved shear stress will not necessarily have to be larger in areas of high stress compared to areas experiencing moderate stress. Note that the shown accumulated slips are for both of the tin grains and that areas having experienced slips will save these throughout the simulation. Consequently, areas of tin which later become fully occupied by IMC also shows plastic slips but the magnitude of the slips do not change when the tin phase is no longer present in the area. This should explain why no visible plasticity is developed along the tin-IMC interface: As the IMC grows it overtakes the areas which would otherwise have had time to develop plastic slips of visible magnitude.

Furthermore this also explains the shape of the plasticized areas which are leaning outwards from the grain boundaries. This is most likely due to the expansion of the IMC semi spheres that initially forms at the triple junctions. During the intermediate stage of the simulation ( $< 10s$ ) they expand, and thus the IMC will overtake areas where plasticity has developed effectively locking their value for the rest of the simulation. As the semi spherical areas expand so will the zones where plasticity develops as the area where transformational strains are present expands with the IMC and it is this that creates the leaning shape of the plasticized areas.

Analyzing the von Mises stress one may note that it is largest close to the tin-IMC interface, which is natural as noted before. The transformational strain associated with the formation of the IMC should cause high stress in its surrounding area. Looking at the different snapshots through time it is also reasonable that the areas of intense stress concentrations are getting smaller as the diffusion of the phases slows down due to the decreasing temperature over time. Thus the transformational strains should become more localized to the boundaries between the copper and the IMC, and between the IMC and the tin respectively as the IMC grows at a slower speed (c.f fig. (22) vs. fig. (24)). In some of the figures (take fig. (13) for example) the stress seems to have a maximum right at the interface boundary, and then shows decreasing stress below it. This is due to the interpolation functions of the two tin phases (c.f.

eq. (22)) As the interpolations functions decrease rapidly when moving further into the IMC so does the stress contribution from the tin phases. Thus it should be noted that the stresses, which here seems to be low in the area where the tin grains and the IMC overlap, are only stress contributions from the tin. According to the Voigt-Taylor assumption the macroscopic stress state in these regions must be obtained through  $\sum_i h_i \bar{\sigma}_i$  but since only stresses in the tin is of interest here, to analyse the plasticity in the tin grains, one should focus on the stress field on, and above, the interface.

Looking at the results from varying the  $\bar{c}$  axis of the middle grain in the  $\bar{x}\bar{z}$ -plane (figs. (5)-(9), and (20)-(24)) one can clearly see that when the middle grain is almost aligned with the side grains,  $\psi = 75^\circ$ , (figs. (20)-(24)) the stress fields as well as the plastic history develops close to symmetrically in both grains. Comparing these results with those where the  $\bar{c}$  axis of the middle grain is almost perpendicular,  $\psi = 30^\circ$ , to the outer grains'  $\bar{c}$  axis (figs. (5)-(9)) one should note that plasticity in the middle grain is minuscule compared to the outer grains. It must be taken into account that the scale of the slips between the simulations is slightly modified when analyzing the figures. This is to resolve areas where plasticity is engaged.

Moving on to the two simulations where the  $\bar{c}$  axis remains in the plane, but where the  $\bar{a}$  and  $\bar{b}$  axes of the middle grain is rotated out of the  $\bar{x}\bar{z}$ -plane. The differences can be seen by looking at stress concentrations which are slightly different for the middle grain having the Bunge-Euler angles  $\phi = 90^\circ, \psi = 30^\circ, \theta = 315^\circ$  (c.f. fig. (16)) compared to the simulation where the middle grain has the angles  $\phi = 90^\circ, \psi = 30^\circ, \theta = 0^\circ$  (c.f. fig. (6)). Another slight difference between the simulations is the magnitude of the accumulated slips. Where the former have slightly larger accumulated slips for a small set of elements (fig. (9) vs. fig. (19)).

Placing the two simulations where the  $\bar{a}$  and  $\bar{b}$  axes of the middle grain is rotated out of the  $\bar{x}\bar{z}$ -plane against one another a slight difference is seen if looking at the stress field in fig. (11) vs. fig. (16). Where in fig. (11) the area of high stress ( $>10$  MPa) is larger than for fig. (16) which also is the most likely cause to why the surrounding material has developed slightly more plasticity.

Redirecting the focus to the grain boundaries no visible plasticity develops there, (fig. (20)-(24)). This is strange as with the model makes no constraint on plasticity to develop on the boundaries and the von Mises stress on the boundaries of the tin grains is large. The model do account for the finite deformation of the crystal by dislocation pile-ups that are modelled to give rise to plastic potential energy, but there is nothing hindering slips from occurring on the boundaries of the crystals. It might be that there are slips occurring but the interpolation functions of the two grains reduce their magnitude to the point where they are no longer visible.

Looking at the figures showing the accumulated slips  $\gamma_{Sn2}^{tot}$  (eq. (20)) of the simulations 5 s in there are some interesting features. Comparing figs. (25a), (25b) and (25c) one may note that as long as the  $\bar{a}$  axis is aligned with the laboratory  $\bar{y}$  axis whilst the  $\bar{b}$  and  $\bar{c}$  axis lie in the  $\bar{x}\bar{z}$ -plane the plasticity developed in the crystal is very slight. It is visible as streaks of light blue running inwards symmetrically towards the centre of the domain.

Redirecting ones attention to fig. (25b) and (25c) one may note that the streaks of blue are more concentrated than for fig. (25a). Especially for fig. (25c) the  $\bar{c}$  axis reside in the  $\bar{x}\bar{z}$ -plane whilst the crystal has its [110]-direction aligned with the  $\bar{y}$ -axis of the laboratory basis. This seems to favour plasticity developing in the crystal as well as displaying a more asymmetric pattern of the streaks of plasticised material. This shows clear signs of the model capturing the dependence of how the slip systems are affecting the plasticity developing within the crystal as one could otherwise have expected a similar patterns as in fig. (25a).

Finally looking at fig. (25d) it has by far the most plasticized material. The underlying mechanism to this is complex. Especially considering the three dimensional stress state imposed by the formation of the IMC. A possible explanation in this specific case could be that the alignment of the tin crystal where its  $\bar{c}$ -axis is directed towards the initial bubble of IMC forming (c.f. fig. (21)) should cause the highest normal stresses as this direction is stiffest in tin (see tab. (2)). This should cause high stresses in the grain which in turn may be favourably projected onto the slip systems of the crystal producing greater amount of plasticized material than for other, less stiff, directions.

## 7 Future Work

First and foremost the crystal plasticity model should be derived in a way known to be thermodynamically admissible and thereafter implemented in MOOSE. The methods currently implemented in MOOSE are usable but for one familiar with C++ these methods should be easy to optimize and to implement in a more general manner as many of the parameters and/or slip system configurations are hard coded in the classes. The tangent used to calculate the stress of the tin (modelled using crystal plasticity finite elements) seems to be poorly implemented as it slows down convergence. Thus there is a possibility of an improvement. Documenting these steps should also be a great asset for coming users as many of the classes implemented in MOOSE lacks documentation. Thus moderate knowledge in C++ is a necessary requirement for using the crystal plasticity and the phase field modules implemented as the only documentation is the code.

The parameter values used for the hardening of the crystals in the simulations were from other authors (see refs. in tab. (4)) but initially a script was constructed so as to curve fit parameters to existing experimental data for stress strain curves of tin along different crystal directions. This is described in the appendix as it was never used partly due to the narrow solution space originating in the stiffness of the equations and partly due to the wide variety of parameters needed to be fitted: From 1 parameter per slip system to 4 or 5 yields very complex minimisation problems containing 32 to 100 parameters to try to find a minimum for. Though this should be elaborated to be automated in a greater degree than was done in this work, and once that is done it should provide a powerful tool for obtaining initial material parameters for numerical models.

Moving on to areas of improvement it must be noted that the plastic potential stated in this work has the parameter value  $Q$  set to equal 1. This is totally arbitrary but stems from the fact that no experimental data to which the used model have been fitted to is known to the author. One could go in line with [17] and connect this parameter to dislocation densities within the crystals and thus enrich the used model further. Another way to approach the value of the parameter is to in line with [26] fit the parameter to known experimental data. The last option though is quite vague. Partly because they use a slightly different potential but also since they arrive at the conclusion that the parameter in itself should be dependent of crystal slips. This would cause their potential to gain yet another factor which is dependent on the internal variables chosen and thus it should also affect the derivation of the same, making their choice somewhat paradoxical and bold as it may disturb the thermodynamical condition set in eq. (45). Luckily the plastic potential in this work has a very low impact as it is quadratic in the slip rates of each phase which in turn are of very low magnitude ( $1E-8$ ), and thus this flaw is neglected.

Furthermore the modelling of the dissipation in this work is obscure as the choice of internal variables and hardening functions are unknown for the model. Instead the result of the choice of these parameters is known: being the flow rule of the slips and the slip resistances, which practically is what is need to be known to implement the model, although the choice made may be in conflict with the dissipation inequality.

Lastly one must note that the temperature dependence of of the elastic parameters was not taken into consideration for the materials in the simulation. Tin for instance, has properties which do change substantially with temperature [14]. Additionally the expression of the state laws (eq. (43)) are derived for an isothermal case and should thus be modified for the model to be more accurate.

Moreover longer simulations should be performed where the plastic history could be saved to better be able to analyse the impact of the IMC growing over the expanded time span as real time periods of tin whiskers growing is on the scale of months or years [3].

Lastly an expression of the free energy functional considering a non-isothermal case is brought up in [19] and should be considered to be implemented in future simulations.

## 8 Conclusions

Due to time limitations combined with the long simulation times simulation of the IMC growth over a longer simulated time span was not achieved. Instead a glimpse of a possible scenario of the IMC forming during manufacture is shown and the stresses this causes in the surrounding material.



Moreover the crystal plasticity model used in this work does capture anisotropic behaviour in tin and the crystal plasticity slip system dependence. It also shows that a multi phase field simulation with incorporated crystal plasticity is possible to execute using the MOOSE software.

# A Appendix

## A.1 Slip systems used for the $\beta$ -tin grains.

Table 6: All the 32 used slip systems of BCT  $\beta$ -Sn. (c.f [14]). The star denotes that the vector is given in reciprocals (Miller indices).

Family of slip systems	slip system nbr.	$\bar{n}_0^*$	$\bar{m}_0$
$\langle 100 \rangle \langle 001 \rangle$	1	(1 0 0)	[0 0 1]
	2	(0 1 0)	[0 0 1]
$\langle 110 \rangle \langle 001 \rangle$	3	(1 1 0)	[0 0 1]
	4	(1 $\bar{1}$ 0)	[0 0 1]
$\langle 100 \rangle \langle 010 \rangle$	5	(1 0 0)	[0 1 0]
	6	(0 1 0)	[1 0 0]
$\langle 110 \rangle \langle 1\bar{1}1 \rangle$	7	(1 1 0)	[1 $\bar{1}$ 1]
	8	(1 1 0)	[ $\bar{1}$ 1 1]
	9	(1 $\bar{1}$ 0)	[1 1 1]
	10	(1 $\bar{1}$ 0)	[ $\bar{1}$ $\bar{1}$ 1]
$\langle 110 \rangle \langle 1\bar{1}0 \rangle$	11	(1 1 0)	[1 $\bar{1}$ 0]
	12	(1 $\bar{1}$ 0)	[1 1 0]
$\langle 100 \rangle \langle 011 \rangle$	13	(0 1 0)	[1 0 1]
	14	(0 1 0)	[1 0 $\bar{1}$ ]
	15	(1 0 0)	[0 1 1]
	16	(1 0 0)	[0 1 $\bar{1}$ ]
$\langle 001 \rangle \langle 010 \rangle$	17	(0 0 1)	[1 0 0]
	18	(0 0 1)	[0 1 0]
$\langle 001 \rangle \langle 110 \rangle$	19	(0 0 1)	[1 1 0]
	20	(0 0 1)	[1 $\bar{1}$ 0]
$\langle 011 \rangle \langle 0\bar{1}1 \rangle$	21	(1 0 1)	[1 0 $\bar{1}$ ]
	22	(1 0 $\bar{1}$ )	[1 0 1]
	23	(0 1 1)	[0 1 $\bar{1}$ ]
	24	(0 1 $\bar{1}$ )	[0 1 1]
$\langle 211 \rangle \langle 0\bar{1}1 \rangle$	25	(1 2 1)	[ $\bar{1}$ 0 1]
	26	(1 $\bar{2}$ 1)	[ $\bar{1}$ 0 1]
	27	( $\bar{1}$ 2 1)	[1 0 1]
	28	( $\bar{1}$ $\bar{2}$ 1)	[1 0 1]
	29	(2 1 1)	[0 $\bar{1}$ 1]
	30	( $\bar{2}$ 1 1)	[0 $\bar{1}$ 1]
	31	( $\bar{2}$ $\bar{1}$ 1)	[0 1 1]
	32	(2 $\bar{1}$ 1)	[0 1 1]

## A.2 Solving for the Hardening Parameters by Solving a System of PDE's

By insertion of eq. (14) and (17) into eq. (16) a system of differential equations of the slip resistance variables is obtained:

$$\dot{s}^\alpha(s^1, \dots, s^\alpha, \dots, s^N) = \sum_{\beta}^N q^{\alpha\beta} h_0 \left| 1 - \frac{s^\beta}{\tau_{sat}^\beta} \right|^c \cdot \text{sgn}\left(1 - \frac{s^\beta}{\tau_{sat}^\beta}\right) \cdot \dot{\gamma}_0 \left| \frac{\tau^\beta}{s^\beta} \right|^{1/m} \quad (82)$$

$$\dot{s}^\alpha(s^1, \dots, s^\alpha, \dots, s^N) = \sum_{\beta}^N q^{\alpha\beta} h_0 \left| 1 - \frac{s^\beta}{\tau_{sat}^\beta} \right|^c \cdot \text{sgn}\left(1 - \frac{s^\beta}{\tau_{sat}^\beta}\right) \cdot \dot{\gamma}_0 \left| \frac{\bar{m}_0^\beta \cdot \bar{M} \cdot \bar{n}_0^\beta}{s^\beta} \right|^{1/m} \quad (83)$$

Exchanging  $\tau^\alpha$  in eq. (82) for the full expression in eq. (15) using the Mandel stress provides the final format as seen in eq. (83).

Insertion of eq. (14) and eq. (15) into eq. (13) results in

$$\dot{\bar{F}}_p = \left( \sum_{\alpha}^N \dot{\gamma}_0 \left| \frac{\bar{m}_0^\alpha \cdot \bar{M} \cdot \bar{n}_0^\alpha}{s^\alpha} \right|^{1/m} \cdot \text{sgn}\left(\bar{m}_0^\alpha \cdot \bar{M} \cdot \bar{n}_0^\alpha\right) \bar{S}_0^\alpha \right) \cdot \bar{F}_p \quad (84)$$

Enabling the components in  $\dot{\bar{F}}_p$  to be written on the form of a system of differential equations:

$$\dot{\bar{F}}_p = \bar{L}_p \cdot \bar{F}_p; \quad \bar{L}_p = \left( \sum_{\alpha}^N \dot{\gamma}_0 \left| \frac{\tau_\alpha}{s^\alpha} \right|^{1/m} \cdot \text{sgn}(\tau_\alpha) \bar{S}_0^\alpha \right) \quad (85)$$

$$\Downarrow$$

$$\begin{bmatrix} \dot{\bar{F}}_{11}^p \\ \dot{\bar{F}}_{12}^p \\ \dot{\bar{F}}_{13}^p \\ \dot{\bar{F}}_{21}^p \\ \vdots \\ \dot{\bar{F}}_{33}^p \end{bmatrix} = \begin{bmatrix} f_1(s^\alpha, \bar{F}_p, \bar{L}_p) \\ f_2(s^\alpha, \bar{F}_p, \bar{L}_p) \\ f_3(s^\alpha, \bar{F}_p, \bar{L}_p) \\ f_4(s^\alpha, \bar{F}_p, \bar{L}_p) \\ \vdots \\ f_9(s^\alpha, \bar{F}_p, \bar{L}_p) \end{bmatrix}; \quad \alpha = 1, 2, 3, \dots, N \quad (86)$$

Thus if  $\bar{F}$  is given as well as initial conditions for the plastic slip resistances  $s^\alpha$ , one may integrate  $\bar{F}_p$  yielding  $\bar{F}_e$  and curve fit to experimental data to obtain the material parameters  $m, \dot{\gamma}_0, c, \tau_{sat}^\alpha$ , and  $h_0$ .

## B Calculation of Derivatives

$$\begin{aligned} \frac{\partial \phi_i}{\partial t} &= -L(\phi) \frac{\delta F}{\delta \phi_i} + \zeta(\bar{r}, t) = -L(\phi) \left[ \frac{\partial F}{\partial \phi_i} - \bar{\nabla} \cdot \frac{\partial F}{\partial \bar{\nabla} \phi_i} \right] + \zeta(\bar{r}, t) \\ &= -L(\phi) \left[ \frac{\partial f_{ch}}{\partial \phi_i} + \frac{\partial f_{int}}{\partial \phi_i} + \frac{\partial f_u}{\partial \phi_i} - \bar{\nabla} \cdot \frac{\partial f_{int}}{\partial \bar{\nabla} \phi_i} \right] + \zeta(\bar{r}, t) \end{aligned} \quad (87)$$

Preliminaries:

$$\frac{\partial h_i}{\partial \phi_j} = \frac{\partial}{\partial \phi_j} \left( \frac{\phi_i^2}{\sum_k \phi_k^2} \right) = \frac{2\phi_i}{\sum_k \phi_k^2} \frac{\partial \phi_i}{\partial \phi_j} + \frac{\phi_i^2 \cdot (-1) \cdot 2\phi_j}{(\sum_k \phi_k^2)^2} = \begin{cases} \frac{-2\phi_j}{\sum_k \phi_k^2} (h_i), & \text{if } i \neq j \\ \frac{-2\phi_j}{\sum_k \phi_k^2} (h_j - 1), & \text{if } i = j. \end{cases} \quad (88)$$

Thus

$$\sum_i \left( \frac{\partial h_i}{\partial \phi_j} \right) = \frac{-2\phi_j}{\sum_k \phi_k^2} \left[ (h_j - 1) + \sum_{i \neq j} (h_i) \right] \quad (89)$$

### B.1 $f_{ch}$

$$\begin{aligned}\frac{\partial f_{ch}}{\partial \phi_i} &= \sum_j \left( \frac{\partial h_j}{\partial \phi_i} f_j + h_j \frac{\partial f_j}{\partial \phi_i} \right); \quad f_j = G_j(x_j)/V_m \\ &= \sum_j \left( \frac{\partial h_j}{\partial \phi_i} f_j + h_j \frac{\partial f_j}{\partial G_j} \frac{G_j}{\partial x_j} \frac{\partial x_j}{\partial h_j} \frac{\partial h_j}{\partial \phi_i} \right)\end{aligned}\quad (90)$$

Using

$$\frac{\partial f_i}{\partial G_i} \frac{G_i}{\partial x_i} = \mu_i, \quad (91)$$

and

$$\begin{aligned}\frac{\partial c}{\partial \phi_i} = 0 &= \frac{1}{V_m} \sum_j \left[ \frac{\partial h_j}{\partial \phi_i} x_j + h_j \frac{\partial x_j}{\partial h_j} \frac{\partial h_j}{\partial \phi_i} \right] \\ &= \frac{1}{V_m} \sum_j \left[ \frac{\partial h_j}{\partial \phi_i} \left( x_j + h_j \frac{\partial x_j}{\partial h_j} \right) \right]\end{aligned}\quad (92)$$

↓

$$0 = x_j + h_j \frac{\partial x_j}{\partial h_j} \Leftrightarrow -x_j = h_j \frac{\partial x_j}{\partial h_j}. \quad (93)$$

Enables eq. (90) to be written on the format

$$\frac{\partial f_{ch}}{\partial \phi_i} = \sum_j \frac{\partial h_j}{\partial \phi_i} (f_j - \mu_j x_j) \quad (94)$$

### B.2 $f_{int}$

$$\begin{aligned}\frac{\partial f_{int}}{\partial \phi_i} &= a_1^{int} \frac{\partial}{\partial \phi_i} \left( \sum_k \left( \frac{\phi_k^4}{4} - \frac{\phi_k^2}{2} \right) + \sum_l \sum_{l \neq k} \left( \frac{a_3^{int}}{2} \phi_k^2 \phi_l^2 \right) + \frac{1}{4} \right) \\ &= a_1^{int} \left( \phi_i^3 - \phi_i + 2a_3^{int} \phi_i \sum_{j \neq i} \phi_j^2 \right)\end{aligned}\quad (95)$$

$$\bar{\nabla} \cdot \frac{\partial f_{int}}{\partial \nabla \phi_i} = \bar{\nabla} \cdot \frac{\partial}{\partial \nabla \phi_i} \left( \frac{a_2^{int}}{2} \sum_j (\nabla \phi_j)^2 \right) = \bar{\nabla} \cdot a_2^{int} \nabla \phi_i \quad (96)$$

### B.3 $f_u$

$$\frac{\partial f_u}{\partial \phi_i} = \frac{\partial}{\partial \phi_i} (f^{(e)} + f^{(p)}) = \frac{\partial}{\partial \phi_i} \left( \sum_j h_j (f_j^{(e)} + f_j^{(p)}) \right) = \sum_j \frac{\partial h_j}{\partial \phi_i} (f_j^{(e)} + f_j^{(p)}) \quad (97)$$

## References

- [1] Kais Ammar et al. “Combining phase field approach and homogenization methods for modelling phase transformation in elastoplastic media.” In: *European Journal of Computational Mechanics/Revue Européenne de Mécanique Numérique* 18.5-6 (2009), p. 485. ISSN: 17797179. URL: <http://ludwig.lub.lu.se/login?url=http://search.ebscohost.com/login.aspx?direct=true&db=edo&AN=ejs27627203&site=eds-live&scope=site>.
- [2] R.J. Asaro and A. Needleman. “Texture development and strain hardening in rate-dependent polycrystals.” In: *Acta Metallurgica* 33.6 (1985), pp. 923–953. URL: <http://ludwig.lub.lu.se/login?url=http://search.ebscohost.com/login.aspx?direct=true&db=inh&AN=2489894&site=eds-live&scope=site>.
- [3] *Basic Information Regarding Tin Whiskers*. Last updated 06/16/2009. URL: <https://nepp.nasa.gov/whisker/background/index.htm>.
- [4] Aritra Chakraborty and Philip Eisenlohr. “A full-field crystal plasticity study on how texture and grain structure influences hydrostatic stress in thermally strained  $\beta$ -Sn films”. In: *Journal of Applied Physics* 124.2 (2018), p. 025302. DOI: 10.1063/1.5029933. URL: <https://doi.org/10.1063/1.5029933>.
- [5] Payam Darbandi et al. “Crystal plasticity finite element study of deformation behavior in commonly observed microstructures in lead free solder joints.” In: *Computational Materials Science* 85 (2014), pp. 236–243. ISSN: 0927-0256. URL: <http://ludwig.lub.lu.se/login?url=http://search.ebscohost.com/login.aspx?direct=true&db=edselp&AN=S0927025614000081&site=eds-live&scope=site>.
- [6] Gordon Davy. *Relay Failure Caused by Tin Whiskers*. Tech. rep. Collected 09/09/2018. Baltimore, MD: Northrop Grumman Electronic Systems, Oct. 2002. URL: [http://nepp.nasa.gov/whisker/refer%20ence/tech\\_papers/davy2002-relay-fa%20ilure-caused-by-tin-whiskers.pdf](http://nepp.nasa.gov/whisker/refer%20ence/tech_papers/davy2002-relay-fa%20ilure-caused-by-tin-whiskers.pdf).
- [7] X. ( 1 ) Deng et al. “Deformation behavior of (Cu, Ag)-Sn intermetallics by nanoindentation.” In: *Acta Materialia* 52.14 (2004), pp. 4291–4303. ISSN: 13596454. URL: <http://ludwig.lub.lu.se/login?url=http://search.ebscohost.com/login.aspx?direct=true&db=edselc&AN=edselc.2-52.0-3242705835&site=eds-live&scope=site>.
- [8] *Design flaw surfaces on PanAmSat’s Galaxy 3R*. Last updated 04/24/2001. URL: <https://spaceflightnow.com/news/n0104/24g3r/>.
- [9] Y. Guan and N. Moelans. “Influence of the solubility range of intermetallic compounds on their growth behavior in hetero-junctions.” In: *Journal of Alloys and Compounds* 635 (2015), pp. 289–299. ISSN: 0925-8388. URL: <http://ludwig.lub.lu.se/login?url=http://search.ebscohost.com.ludwig.lub.lu.se/login.aspx?direct=true&db=edselp&AN=S0925838815004545&site=eds-live&scope=site>.
- [10] Johan Hektor et al. “Coupled diffusion-deformation multiphase field model for elastoplastic materials applied to the growth of Cu<sub>6</sub>Sn<sub>5</sub>”. In: *Acta Materialia* 108 (Feb. 2016), pp. 98–109.
- [11] R. Hill. “Elastic properties of reinforced solids: Some theoretical principles.” In: *Journal of the Mechanics and Physics of Solids* 11.5 (1963), pp. 357–372. ISSN: 00225096. URL: <http://ludwig.lub.lu.se/login?url=http://search.ebscohost.com/login.aspx?direct=true&db=edselc&AN=edselc.2-52.0-6544226089&site=eds-live&scope=site>.
- [12] S.R. Kalidindi, C.A. Bronkhorst, and L. Anand. “Crystallographic texture evolution in bulk deformation processing of FCC metals.” In: *Journal of the Mechanics and Physics of Solids* 40.3 (1992), pp. 537–569. URL: <http://ludwig.lub.lu.se/login?url=http://search.ebscohost.com/login.aspx?direct=true&db=inh&AN=4146692&site=eds-live&scope=site>.
- [13] Yoshiharu Kariya, Sho Tajima, and Saori Yamada. “Influence of Crystallographic Orientation on Fatigue Reliability of beta-Sn and beta-Sn Micro-Joint”. In: *MATERIALS TRANSACTIONS* 53.12 (2012), pp. 2067–2071. DOI: 10.2320/matertrans.MB201204.

- [14] Tae-Kyu Lee et al. *Fundamentals of Lead-Free Solder Interconnect Technology. [Elektronisk resurs] : From Microstructures to Reliability*. Boston, MA : Springer US : Imprint: Springer, 2015., 2015. ISBN: 9781461492665. URL: <http://ludwig.lub.lu.se/login?url=http://search.ebscohost.com/login.aspx?direct=true&db=cat01310a&AN=lovisa.004826807&site=eds-live&scope=site>.
- [15] Elmquist Lennart. “Tennwhisker”. MA thesis. Lunds Faculty of Engineering, 2004.
- [16] Z. Mei, A.J. Sunwoo, and Jr. Morris J.W. “Analysis of low-temperature intermetallic growth in copper-tin diffusion couples.” In: *Metallurgical Transactions A (Physical Metallurgy and Materials Science)* 23A.3 (1992), pp. 857–864. URL: <http://ludwig.lub.lu.se/login?url=http://search.ebscohost.com/login.aspx?direct=true&db=inh&AN=4158567&site=eds-live&scope=site>.
- [17] Ylva Mellbin, Håkan Hallberg, and Matti Ristinmaa. “An extended vertex and crystal plasticity framework for efficient multiscale modeling of polycrystalline materials”. In: *International Journal of Solids and Structures* 125 (2017), pp. 150–160. ISSN: 0020-7683. DOI: <https://doi.org/10.1016/j.ijsolstr.2017.07.009>. URL: <http://www.sciencedirect.com/science/article/pii/S0020768317303268>.
- [18] N. Moelans. “A quantitative and thermodynamically consistent phase-field interpolation function for multi-phase systems.” In: *Acta Materialia* 59.3 (2011), pp. 1077–1086. ISSN: 13596454. URL: <http://ludwig.lub.lu.se/login?url=http://search.ebscohost.com/ludwig.lub.lu.se/login.aspx?direct=true&db=edselc&AN=edselc.2-52.0-78650706888&site=eds-live&scope=site>.
- [19] Nele Moelans, Bart Blanpain, and Patrick Wollants. “An Introduction to Phase-Field Modeling of Microstructure Evolution”. In: 32 (June 2008), pp. 268–294.
- [20] *Multiphysics Object Oriented Simulation Environment (MOOSE)*. 2009. URL: <http://www.mooseframework.org/>.
- [21] M. Ortiz and E.a. Repetto. “Nonconvex energy minimization and dislocation structures in ductile single crystals.” In: *Journal of the Mechanics and Physics of Solids* 47 (1999), pp. 397–462. ISSN: 0022-5096. URL: <http://ludwig.lub.lu.se/login?url=http://search.ebscohost.com/ludwig.lub.lu.se/login.aspx?direct=true&db=edselp&AN=S0022509697000963&site=eds-live&scope=site>.
- [22] C. Shen, J.P. Simmons, and Y. Wang. “Effect of elastic interaction on nucleation: II. Implementation of strain energy of nucleus formation in the phase field method”. In: *Acta Materialia* 55.4 (2007), pp. 1457–1466. ISSN: 1359-6454. DOI: <https://doi.org/10.1016/j.actamat.2006.10.011>. URL: <http://www.sciencedirect.com/science/article/pii/S1359645406007336>.
- [23] Ellad B. Tadmor and Ronald E. Miller. *Modeling Materials. [Elektronisk resurs] : Continuum, Atomistic and Multiscale Techniques*. Cambridge : Cambridge University Press, 2011, 2011. ISBN: 9781139003582. URL: <http://ludwig.lub.lu.se/login?url=http://search.ebscohost.com/login.aspx?direct=true&db=cat01310a&AN=lovisa.004268471&site=eds-live&scope=site>.
- [24] Fuqian Yang and J. C. M. Li. “Deformation behavior of tin and some tin alloys.” In: *JOURNAL OF MATERIALS SCIENCE-MATERIALS IN ELECTRONICS* 18.1-3 (), pp. 191–210. ISSN: 09574522. URL: <http://ludwig.lub.lu.se/login?url=http://search.ebscohost.com/login.aspx?direct=true&db=edswsc&AN=000242853600013&site=eds-live&scope=site>.
- [25] A. Zamiri, T.R. Bieler, and F. Pourboghra. “Anisotropic crystal plasticity finite element modeling of the effect of crystal orientation and solder joint geometry on deformation after temperature change.” In: *Journal of Electronic Materials* 38.2 (2009), pp. 231–240. URL: <http://ludwig.lub.lu.se/login?url=http://search.ebscohost.com/login.aspx?direct=true&db=inh&AN=10613717&site=eds-live&scope=site>.
- [26] L. ( 1 ) Zhao et al. “On the plastic driving force of grain boundary migration: A fully coupled phase field and crystal plasticity model.” In: *Computational Materials Science* 128 (2017), pp. 320–330. ISSN: 09270256. URL: <http://ludwig.lub.lu.se/login?url=http://search.ebscohost.com/login.aspx?direct=true&db=edselc&AN=edselc.2-52.0-85003806594&site=eds-live&scope=site>.